International Journal of Material Science (IJMSCI) Volume 4 Issue 3, September 2014 www.ij-ms.org
doi: 10.14355/ijmsci.2014.0403.01

Synthesis and Characterization of Poly (Vinyl Acetate)/MMT Nanocomposite Flame Retardant

Mamata Sahu[1], Ramakanta Samal[2], Trinath Biswal[3], Prafulla K Sahoo[1]*

[1]Department of Chemistry, Utkal University, Vani Vihar, Bhubaneswar 751004, India

[2]Department of Chemistry, Rajendra College, Bolangir 767002, India

[3]Department of Chemistry, VSS University of Technology, Burla 768018, India

psahoochemuu@gmail.com

Abstract

Current environmental benign and flame retardant poly (vinyl acetate) (PVAc)/montmorillonite (MMT) clay nanocomposites were prepared by emulsifier free emulsion technique in microwave (MW) oven. MMT clay was incorporated as additional filler in PVAc/MMT nanocomposites to improve the homogeneity of the 'physical' barrier, since clay produces silicon-oxy-carbide (Si–O–C) char on heating. The fine dispersion of the MMT and the interactions between PVAc and clay created significant improvement of the flame retardancy which has been evaluated using cone calorimeter. The presence of clay in PVAc/MMT nanocomposites was characterized with infrared (IR), X-ray diffraction (XRD) and transmission electron microscopy (TEM). The fire retardancy of PVAc/MMT nanocomposites caused by the formation of Si–O–C char was characterized byscanning electron microscopy (SEM). The biodegradation property was tested by activated sludge water via water absorbency and was further confirmed from SEM for its better commercialization and ecofriendly nature.

Keywords

Emulsifier Free Emulsion; Microwave; Nanocomposites; Flame Retardant; Biodegradation

Introduction

Polymer-clay nanocomposites have become one of the most popular nanocomposites, since Nylon-6/MMT nanocomposites were invented by Toyota research group in 1993 [Kojima *et al 1993*]. Various polymers [Aminabhavi *et al 1987 and 1989]* clays, processes and characterizations associated with the polymer-clay nanocomposites have been reported in the last few decades. Most of the results suggested that only a few weight percentage of clay can effectively improve strength, thermal stability and gas barrier properties.

In our previous papers, we prepared PBA/SS [Sahoo, Prafulla K, Mohapatra Rumki *2003*], PAN/SS [Sahoo, Prafulla K, Samal, Ramakanta, Swain, Sarat K and Rana, Pradip K. *2008*] nanocomposites, and PMMA Samal, Ramakanta and Sahoo Prafulla K *2006* D nanoparticles by emulsifier free emulsion polymerization method, a clean and prevailing method for manufacture of polymeric lattices. It is also easier to dissipate heat than other polymerization methods. Recently, we have successfully adopted the emulsifier free emulsion polymerization to fabricate the PMMA/MMT nanocomposites, simply by intercalating the PMMA into MMT with an initiator potassium monopersulfate (KMPS Sahoo, Prafulla K and Samal, Ramakanta *2007*D. However the PMMA/MMT nanocomposite latex particles are too rigid to form a film by casting, so their applications are limited in packaging, adhesive and coating industries. And for better application in these fields PVAc and its nanocomposites have long been used. PVAc and its copolymers have advantage over these templates due to the maintenance of the superstructures of the monomers during the polymerization Warson H and Finch CA *2001*.

The study of polymer/clay nanocomposites with superior thermal, mechanical and barrier properties as compared to virgin polymer Bhat, Santoshkumar D and Aminabhavi, Tejraj M *2006* D has become more attractive by recent demonstrations Kumar, Annamalai P, Depan, Dilip, Tomer, Namrata S and Singh Raj P 2009 *and* Zhang, Xingui and Loo, Leslie S. *2009* D of their flame retardant properties, namely a significant decrease in the peak heat release rate (PHRR), a change in the char structure, and a decrease in the rate of mass loss during combustion in a cone calorimeter Sahoo, Prafulla K and Samal, Ramakanta *2007*, Porter D, Metcalfe E, Thomas MJK *2000*D *and* Gilman, Jeffrey W.*1999*D. Polymer-clay nanocomposi-

tes are believed to be a new promising approach in fire retardancy due to their great potential in forced flaming conditions, for instance, the reduction of the flame spread and fire propagation. The Si–O–C char were first formed on polymer-clay nanocomposites which improved their thermal and fire retardant properties due to their great potential in forced flaming conditions, for instance, the reduction of the flame spread and fire propagation. The most dominant mechanism in their improved fire retardancy is the accumulation of clay layers at the combusting surface of the condensed phase serving as a barrier to O_2 supply and the pyrolysis gases.

Previously, PVAc/MMT nanocomposites have been prepared by bulk radical Liu, Pinggui, Gong, Kecheng, Xiao, Peng and Xiao, Min*2000*., melt blending Gelfer *et al 2005*, soap-free emulsion Chien, An-T and Lin, King-F *2007* polymerization methods by using additives/fillers like graphite oxide Liu, Pinggui, Gong, Kecheng, Xiao, Peng and Xiao, Min. *2000*, southern clay Duquesne, S, Jama, C, Bras, ML, Delobel, R, Recourt P and Gloaguen, JM*2003*, multi-walled nanotube Duquesne, S, Jama, C, Bras, ML, Delobel, R, Recourt P and Gloaguen, JM *2004*, bentonite clay Preston, Christopher ML, Amarasinghe, Gandara, Hopewell, Jefferson L, Shanks, Robert A and Mathys Zenka.*2004* , etc and also their various properties were studied. But to the best of our knowledge no research group in the available literature has employed the flame retardant properties and the role of clay in PVAc/MMT nanocomposites.

Further, studies on green polymeric materials, which avoid the use of any toxic or noxious components in their manufacture and could be naturally biodegradable, are in demand as they reduce the hazardous effect of plastics and other polymeric compounds on environment.

Experimental Materials

Vinyl acetate (VAc), was distilled under reduced pressure before being used to remove the inhibitor. The initiator, potassium monopersulfate (KMPS) (Acros), was directly used and all other reagents were from E. Merck, India (AR grade) and were used after purification by standard techniques. MMT clay with cation exchange capacity (CEC) of 90-mequiv/100 g was from Himedia India Ltd.

Synthesis of PVAc/MMT Nanocomposite

The microwave reactor was reconstructed from a Whirlpool T120 microwave oven. The electromagnetic energy was produced by a magnetron at 2.45 GHz; the power could be adjusted between 0 and 700 W continuously. The temperature of the reaction system was monitored with an IR temperature pickup. With an internal cooling flask, the temperature could be adjusted precisely and independently of the microwave power in microwave-assisted polymerization by taking known amount of distilled VAc in 4/5th part deionised water via stirring with *in situ* developed $CuSO_4$ (0.1M)/EDTA (0.1M) complex. At the same time, desired amount of MMT was dispersed in rest 1/5th part of water at same condition for 1 min with constant stirring. The MMT suspension was added to the reaction vessel containing VAc and stirred with constant velocity at 400 to 600 rpm in N_2 atmospheric pressure, and then the flask was heated with 700 W microwave irradiation. After a temperature of 60°C was attained in 1 min, the microwave power was reduced to 40 W to maintain the temperature. Then requisite amount of initiator KMPS solution was carefully injected to the reaction mixture. The polymerization was accomplished in 2 h. Then the polymerization was terminated by the addition of 0.1 M ferrous ammonium sulfate solution keeping the reaction vessel in ice cold water. The precipitate polymers were filtered and purified by washing with distilled water and toluene. Then it was dried at 40 ^{0}C in vacuum oven till a constant mass was formed.

Characterization

The IR spectra of PVAc (degree of polymerization, ~3600), and PVAc /MMT nanocomposite, in the form of KBr pellets were recorded with Perkin-Elmer model Paragon-500 FTIR spectrometer. The interaction of PVAc into the silicate layer was confirmed by using a XRD monitoring diffraction on Philips PW-1847 X-ray crystallographic unit equipped with a Guinier focusing camera CuK_2 radiation. Nanoscale structure and surface morphology of PVAc/MMT were investigated by means of TEM (H-7100 Hitachi Co), operated at an accelerating voltage of 100 Kv and SEM JEOL Ltd, Japan model 5200 SEM, coating it with gold at different magnifications.

Thermal properties were measured by using a Shimadzu DTA-500 system. It was carried out in air from room temperature to 600^0 C at a heating rate of 10^{0}C/min.

The fire performance of the PVAc/MMT

nanocomposites were evaluated in a horizontal orientation using a Cone Calorimeter Zanetti, M, Kashiwagi, T, Falqui, L and Camino G. *2002* in accordance with the procedure Lewin *et al 2003* outlined in AS/NZS 3837:1998, which was based on ISO 5660-1:1993, with dimensions 100 x 100 x 4 mm^3 at a heat flux of 35 kWm^{-2}. All the specimens were tested in triplicate using a retaining frame with data collection intervals of 5s. The combustion parameters determined include time to ignition (TTI), rate of heat release (HRR), total heat released (THR), effective heat of combustion, mass loss rate (MLR), carbon monoxide and carbon dioxide yield.

In TTI, time required for the entire surface of the sample is to burn with a sustained luminous flame, whereas in peak heat release rate (PHRR), it expresses the maximum intensity of a fire Weil, Edward D, Patel, Navin G, Said, MM, Hirschler, Macrelo M, and Shakir, S *1992* indicating the rate and extent of fire spread. Fire Performance Index, FPI (m^2s/kW)—defined as the ratio of TTI to PHRR that is parameter related with the time to flashover (or the time available for escape) in a full-scale fire situation Hirschler, MM and Shakir, S. *1992*.

Parameters related with the smoke evolution were also obtained, such as total smoke released (TSR) calculated by integrating the smoke released rate (SRR), average of CO (Av.CO) emission, CO/CO_2 weight ratio and smoke density, measured by the decrease in transmitted light intensity of a helium neon laser beam photometer, and expressed in terms of average smoke extinction area (Av.SEA). Smoke Parameter, SP (MW/kg) is defined as the product of Av.SEA and PHRR. This parameter is indicative of the amount of smoke generated in a fire situation Scudamore, MJ, Briggs, PJ and Prager FH*1991*

Tensile bars of PVAc/MMT were obtained on a Van Dorn 55 HPS 2.8 F mini injection molding machine under the following processing conditions: a melt temperature of 150 ºC, a mold temperature of 25 ºC, an injection speed of 40 mm/s, an injection pressure of 10 MPa, a holding time of 2 s, with a total cycle time of 30 s. Tensile measurements on injection molded samples of nanocomposites were performed according to ASTM D-638-00 using an Instron test machine Model 5567. Tests were carried out at a crosshead speed of 50 mm/min and a 1 kN load cell without the use of an extensometer. All tests were performed at room temperature and the results were the average of five measurements. The highest value of standard deviation was 15%.

The activated sludge water was collected from tank areas receiving toilet and domestic wastewater. In most areas of our country, the waste materials after use are dumped usually near the sludge and the sludge water contains many microorganisms (bacteria, fungi, yeast, etc,) responsible for the biodegradation of waste materials. The sludge was collected Federle *et al 2002* in a polypropylene container, which was filled completely and then fully closed. Then, the wastewater was brought to the lab immediately. After settling for about 1h, the total solid concentration was increased to 5000 mg/L. The activated sludge water and a polymer sample (0.2g) were incubated together in a sterilized vessel at room temperature (28± 2^0C). Duplicate samples were removed at time intervals for biodegradation study via weight loss. Vessels containing polymer samples without sludge water were treated as controls Liu, Ying-L, Hsu, Chih-Y and Hsu Keh-Y.*2005*

Results and Discussion

From the series of experiments, it was found that the PVAc was exfoliated into gallery structure of silicate by the catalytic action of Cu(II)/EDTA complex with help of the initiator KMPS in MW oven. The complex initiating system helps to stabilize the emulsion latex to a high conversion level in the absence of emulsifier. The initiation is a surface catalysis with adequate energy transfer from the complex to the initiator KMPS, resulting in a complex initiation mechanism deviating from a simple path of decomposition.

Infrared Spectra (FTIR)

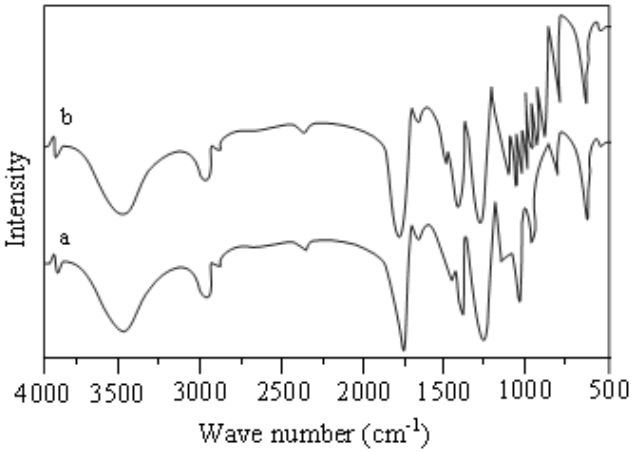

FIGURE 1. FTIR OF (A) PVAc AND (B) PVAc/MMT (5% w/v) (S_5) NANOCOMPOSITE.

A representative FT-IR spectrum of a sample is illustrated in Fig. 1. The peak at 1739 cm^{-1} >C=O, and characteristic peaks at 1239, 1020 cm^{-1} C–O, and 1375

cm^{-1} CH_3 corresponding to PVAc are clearly seen. In Fig. 1(b), the Si–O–Si bond stretching showed peak at 850–1050 cm^{-1} which was absent in Fig. 1(a), indicating the presence of silicate in the PVAc/MMT nanocomposite matrix.

X-ray Diffraction (XRD)

The systematic arrangement of the silicate layers of the intercalated/exfoliated nanocomposites has been elucidated by XRD in calculating interlayer spacing with the help of Bragg's equation. Due to the intercalation of PVAc into galleries of silicate of MMT via emulsion polymerization, the d-spacing of PVAc/MMT nanocomposites increased with shifting of 2θ to lower values. The XRD pattern of PVAc/MMT nanocomposites as shown in Fig. 2 (c) indicated the complete disappearance of clay peak which concluded the better dispersion and exfoliation of silicate layers over PVAc matrix at lower concentration i.e. ≤ 5% w/v of MMT. If the concentration of MMT is increased in PVAc matrix, then exfoliated structure is changed to intercalated structure as shown in Figure 2 (b), which has been explained in our previous paper Sahoo, Prafulla K and Samal, Ramakanta *2007* and further evidence from corresponding TEM Figure 3 (a) and (b).

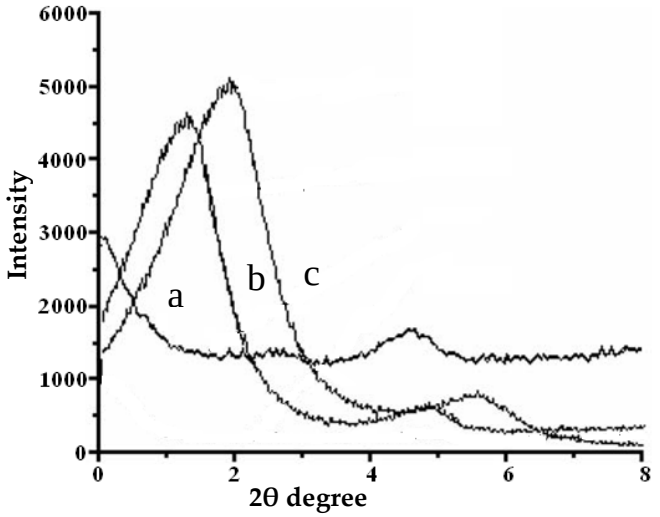

FIGURE 2: XRD OF PVAc/MMT NANOCOMPOSITES (A) 5 % AND (B) 10 % w/v AND (C) PURE MMT CLAY.

Transmission Electron Microscopy (TEM)

TEM studies are necessary to verify the extent of exfoliation/intercalation achieved as shown in Figure 3 (a) and (b) for 5 wt % and 10 wt % samples. In Figure 3 (a) and (b), it is shown that the MMT layers are well dispersed in the PVAc matrix. Although the MMT layers still retain their orientation to some degree, the MMT are highly delaminated into some thin lamellas by PVAc with a dimension of about 1~2 nm in thickness when MMT content is ≥ 5 %, the layered structure of the MMT is generally intercalated in the polymer matrix (Fig. 3(a)). But at lower concentration of MMT i.e. ≤ 5%, the silicate layer fully destroy their orientation, which have good agreement with their XRD. On the basis of the evidence from XRD and TEM, the PVAc/MMT nanocomposites with a highly exfoliated or intercalated structure have been successfully prepared via an in situ intercalation process in the neutral aqueous media.

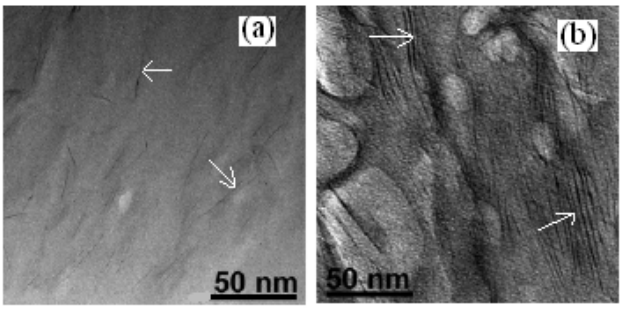

FIGURE 3. TEM OF (A) PVAc/MMT (5% w/v), (B) PVAc/MMT (10% w/v) NANOCOMPOSITES.

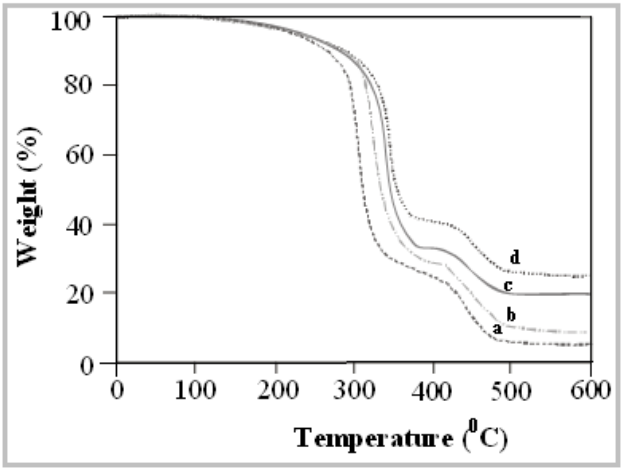

FIGURE 4. TGA OF (A) PVAc, (B) PVAc/MMT (5% w/v), (C) PVAc/MMT (10% w/v) AND (D) PVAc/MMT (15% w/v) NANOCOMPOSITE.

TG Analysis

The thermal properties of the nanocomposite materials have been evaluated by TGA as shown in Figure 4. The difference between decomposition temperature (T_d) of the nanocomposite and that of the free polymer became more pronounced as the silicate content was increased. In contrast to PVAc, the onset of decomposition for PVAc/MMT nanocomposites is shifted towards a higher temperature with inclusion of MMT, indicating an enhancement of the thermal stability upon intercalation. The PVAc/MMT nanocomposite exhibited higher thermal stability due

to the higher decomposition onset temperature than that of PVAc, which can be attributed to the nanoscale silicate layers preventing out-diffusion of the volatile decomposition product Chalais, Stephane, Laszlo, Pierre and Mathy and Arthur*1986*. On the other hand, since the inorganic part (silicate) of the nanocomposite film almost did not lose its weight during the heating period, the shift of weight loss to higher temperature region might be simply due to that the nanocomposite films possessed relatively small amount (about 4 wt %) of organic polymer that contributed to the weight loss.

Cone Calorimeter

Flame retardant mechanism of PLSN by physical barrier methods is due to the formation of Si–O–C (carbonaceous-silicate) char, which acts as insulating barrier for flow of heat and mass. Out of various methods TTI is one which defines the time that a material can withstand the heat flux radiated by a fire before it experiences sustained flaming combustion. It was found from Table 1 and Figure 5, that, the TTI of the PVAc/MMT nanocomposites were lower than virgin PVAc i.e., ignition times for nanocomposites were lower than virgin polymer due to the first decomposition of MMT clay at lower temperature present in nanocomposites correlated with previous report Sahoo, Prafulla K and Samal, Ramakanta *2007*, Ray, Suprakash S, Okamoto, Kazuaki and Okamoto Masam*2003*.

PHRR is one of the most important parameters associated with the flammability and combustion of materials. The samples which have low value of PHRR are better fire retardants than those of high HRR value. The HRR value PVAc/MMT nanocomposites was observably decreased even in the presence of **a** small amount of silicate. It was found from Table 1 and Figure 5, that the PHRR value of virgin polymer was more than any PVAc/MMT nanocomposites. Due to the formation of Si–O–C ceramic char residue (Fig. 4 (f, g)) by MMT present in PVAc/MMT, nanocomposites (PLSN) act as an insulating protective barrier by reducing the heat and mass transfer between the flame and sample, which has been explained by Gilman, Jeffrey W, Kashiwagi, T.*2000* and also explained in Figure 5. Further, with increasing % of MMT content in the polymer nanocomposites, the HRR values decreased as shown in Figure 5 (b-d) curves. The reduction of PHRR (Δ) values was proportional to the fraction of clay present in the nanocomposite at low concentrations Gilman, Jeffrey W1999 1999 but the rate of decrease of PHRR value was approximately independent of % of MMT clay at higher concentration was explained in our previous paper PMMA/MMT nanocomposite Sahoo, Prafulla K and Samal, Ramakanta*2007*, also given by Gilman, Jeffrey W, Kashiwagi, T, Giannelis, EP, Manias, E, Lomakin, S, Lichtenhan, JD and Jones P. 1998. Total heat released (THR) is a factor which means the total amount of heat evolved during combustion. In the figure the area occupied by the curve is known as THR. From Fig. 5 and Table 1, it is found that the THR values of PVAc/MMT nanocomposites are lower than that of virgin PVAc and decrease is independent of MMT content at higher concentration i.e. ≥ 10% that means are occupied by the curve is same.

TABLE 1 CONE CALORIMETER DATA OF PVAC/MMT NANOCOMPOSITES

Samples	TTI (s)	PHRR kWm^{-2}	THR MJm^{-2}	MLR $g/s)x10^{-3}$	Av.CO (kg/kg)	PSEA (m^2/kg)
PVAc+0% w/v MMT(S_0)	63±3	887±20	68±5	56±5	3.8	228
PVAc+5% w/v MMT(S_5)	48±3	614±19	64±5	43±5	3.0	363
PVAc+10% w/v MMT(S_{10})	46±3	482±19	63±5	41±5	2.9	406
PVAc+15% w/v MMT(S_{15})	44±3	412±19	63±5	40±5	2.8	489

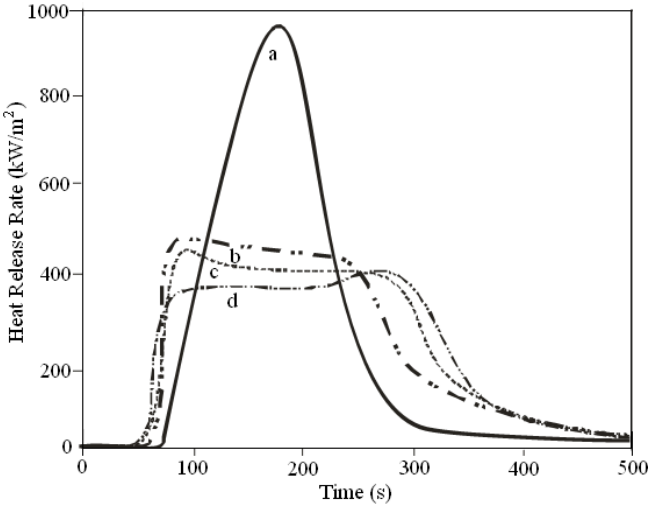

FIGURE 5. HEAT RELEASE RATE CURVE OF (A) PVAc, (B) PVAc/MMT (5% w/V), (C) PVAc/MMT (10% w/V) AND (D) PVAc/MMT (15% w/V) NANOCOMPOSITES.

The mass loss rate (MLR) is a measure of the extent of thermal decomposition and subsequent volatilization of a combustible material in fire. The relationship between the MLR and HRR is linear i.e., it is another factor which describes the fire retardant properties **or** the heat release capacity depends on the maximum mass loss rate or the heat of combustion of the decomposition products at that temperature. From Table 1, it is found that the MLR value of PVAc/MMT nanocomposites has decreased, with the addition of

MMT in the virgin polymer and this decrease with increasing % of MMT. The value was correlated with the rate of mass loss from a polymer-silicate hybrid when exposed to heat, which was significantly reduced compared with the pure polymerLe, BM, Camino, G, Bourbigot, S and Delobel, R*1998*.

Additionally, several other parameters were measured simultaneously during the cone calorimetry experiments. Those included measurement of the effective heat of combustion, specific extinction area (SEA) (smoke emission) and carbon monoxide and carbon dioxide emissions. Carbon monoxide is recognized as one of the most toxic gaseous products in fires and is a reaction product of the incomplete combustion of volatiles at the fire/composite boundary. It can also be a by-product of the decomposition of certain polymers. From Table 1, it was observed that the decrease of average CO (AvCO) in case of nanocomposite is due to the lower PHRR is explained by Mouritz, AP, Mathys, Z and Gibson, AG 2006. The decrease in the peak smoke emission is due to the presence of the organoclay which causes the decreases of PHRR, suggesting that the char layer that was formed prevented the degradation.

Mechanical Properties

The mechanical properties, including Young's modulus, toughness, yield stress and strain of all the nanocomposites prepared in this study, together with the corresponding values of the virgin polymer are shown in Figure 6 (a). All the nanocomposites exhibit post yield elongation. The Young's modulus and tensile strength are plotted in Figure 6 (b) as a function of clay content. Both the Young's modulus and tensile strength steadily increased with clay content. It is noteworthy that tensile modulus increases by 30% and tensile strength by 16% with the addition of 5 wt% clay to PVAc, which is consistent withKojima, Y, Usuki, A, Kawasumi, M, Okada, A, Fukushima, Y, Kurauchi, T and Kamigaito, O. *1993*. The role of clay as a reinforcing agent in PVAc matrix is clearly manifested. The property implying that interfacial bonding between layered silicates and PVAc is stronger. However, a comprehensive understanding of the interfacial interaction between PVAc and MMT is lacking. It has been believed that the higher parity between the surface polarities of PVAc and MMT leads to platelet exfoliation of clay among the polymer matrix, resulting in more efficient reinforcement effect. The toughness of nanocomposites decreased tremendously with increasing silicate content which is in accordance with our previous work PBA/SS Sahoo, Prafulla K, Samal, Ramakanta, Swain, Sarat K and Rana, Pradip K *2008*and also the results obtained earlier Swain Sarat K and Isayev AI *2007*

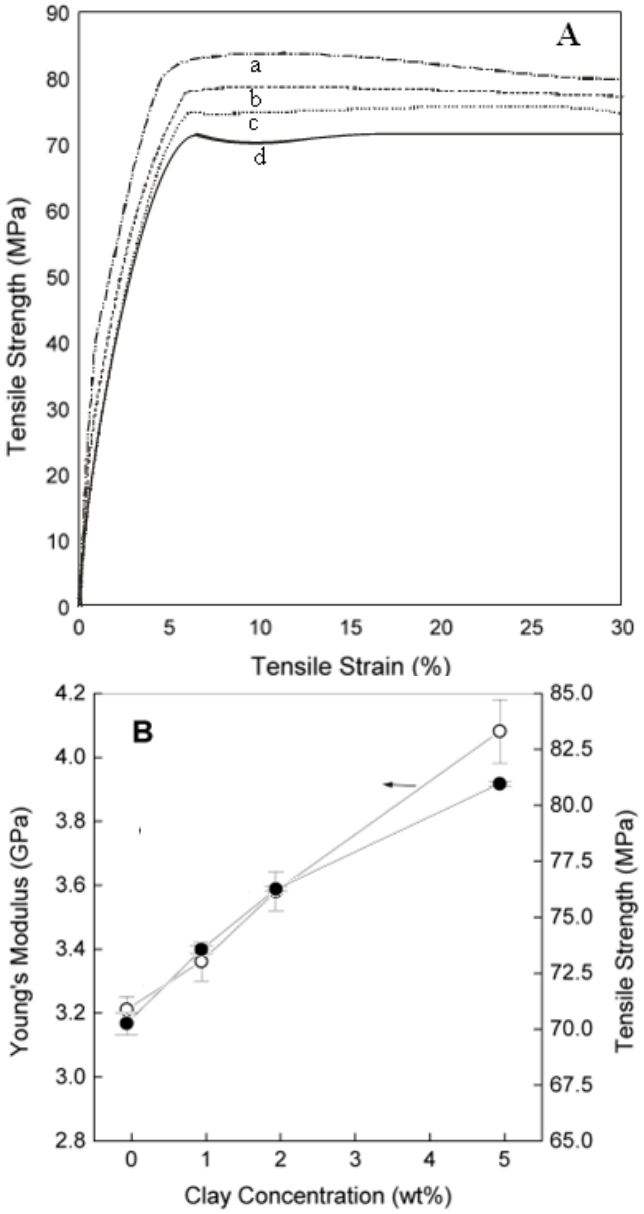

FIGURE 6. (A) STRESS–STRAIN CURVES FOR PVAc AND ITS CLAY NANOCOMPOSITES AT A CROSSHEAD SPEED OF 5 mm/min; (B) TENSILE MODULUS (E) AND YIELD STRENGTH OF PVAc/CLAY NANOCOMPOSITES AS A FUNCTION OF CLAY CONCENTRATION.

Biodegradation

Biodegradation by activated sludge is less in case of PVAc than that of PVAc/MMT nanocomposites. The biodegradation is increased with increasing percentage of MMT (Table 2). From this observation, it was confirmed that the growth of microorganisms are more in case of nanocomposite due to the presence of hydrophilic MMT content. The percentage weight loss

of nanocomposites is more than the hydrophobic PVAc. The water absorbency is less in case of PVAc, which results in its reducing the biodegradation. The SEM Figure 7 of PVAc/MMT shows more networking surface and regular but, after biodegradation, the surface seems to be rough and unclear, which confirm the microorganisms mediated degradation of the PVAc/MMT nanocomposite.

TABLE 2 BIODEGRADATION OF PVAC/MMT NANOCOMPOSITES BY ACTIVATED SLUDGE WATER

Sample Code No.	% of Weight Loss Days				Water Absorbency Q (g H_2O/g Sample)
	1	8	15	30	
S_0	2.11	7.22	15.41	20.40	21
S_5	7.14	14.48	29.87	41.78	43
S_{10}	8.58	18.24	31.42	54.98	56
S_{15}	10.64	21.64	36.48	60.94	64

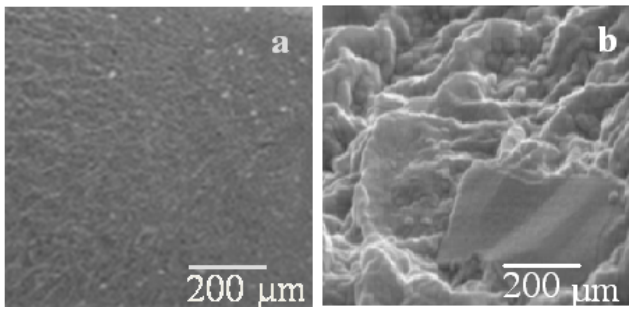

FIGURE 7. SEM OF PVAC/MMT NANOCOMPOSITE (A) BEFORE AND (B) AFTER BIODEGRADATION 30 DAYS.

Conclusion

PVAc/MMT nanocomposites were prepared by novel, cost effective, non-conventional emulsifier free emulsion technique in MW oven. XRD results showed a disorder layer structure due to intercalation/exfoliation of polymer into the layered silicate is further conformed by TEM analysis. These composites are further characterized by TGA and exhibited improved properties of thermal stability with good fire retardant properties. The developed novel flame retardant PVAc/MMT nanocomposites exhibits significant properties thereby inducing hydrophilic character to hydrophobic matrix and most importantly, shows good biodegradebility. To conclude, as the synthesized nanocomposites are ecofriendly environmental benign green synthesis by MW, they may open the door for future prospects as commercial flame retardants.

REFERENCES

Aminabhavi, Tejraj M, Cassidy, Patrick E and Biradar, Ningond S. "Versatile Lightweight Polymer Composites". J Macro Sci Part C: Polym Rev 3-4 (1987): 459-503.

Aminabhavi, Tejraj M and Cassidy, Patrick E. "Flammability Characteristics of Polymers". Polym Plast Techn Enginer 7-8 (1989): 717-51.

Bhat, Santoshkumar D and Aminabhavi, Tejraj M. "Novel Sodium Alginate–Na+MMT Hybrid Composite Membranes for Pervaporation Dehydration of Isopropanol, 1,4-Dioxane and Tetrahydrofuran". Separation and Purification Techno 51 (2006): 85–94.

Chalais, Stephane, Laszlo, Pierre and Mathy and Arthur. "Catalysis of the cyclohexadienone-phenol rearrangement by a Lewis-acidic clay system". Tetrahedron Lett 27 (1986): 2627-2630.

Chien, An-T and Lin, King- F. "Morphology and Permeability of Exfoliated PVAc-MMT Nanocomposite Films Cast from Soap-Free Emulsion-Polymerized Latices". J Polym Sci Part A: Polym Chem 45 (2007): 5583-89.

Duquesne, S, Jama, C, Bras, ML, Delobel, R, Recourt P and Gloaguen, JM. "Elaboration of EVA–Nanoclay Systems—Characterization, Thermal Behaviour and Fire Performance". Compos Sci Technol 63 (2003): 1141–48.

Federle, Thomas W, Barlaz, Mortan A, Pettugrew, Charles A, Kerr, Kathy M, Kemper, Joseph J, Nuck Barbar A and Lee A. Schechtman. "Anaerobic Biodegradation of Aliphatic Polyesters: Poly (3-Hydroxybutyrate-Co-3-Hydroxyoctanoate) and Poly (E-Caprolactone)". Biomacromolecules 3 (2002): 813–22.

Gelfer, Mikhail Y, Burger, Christian, Chu, Benjamin, Hsiao, Benjamin S, Drozdov, Aleksey D, Si, Mayo, Rafailovich, Miriam, Sauer, Bryan B and Gilman, Jeffrey W. . "Relationships Between Structure and Rheology in Model Nanocomposites of Ethylene-Vinyl-Based Copolymers and Organoclays". Macromolecules 38 (2005): 3765-75.

Gilman, Jeffrey W, Kashiwagi, T, Giannelis, EP and Lichtenhan, JD. "Nanocomposites: A Revolutionary New Flame Retardant Approach.". SAMPE J. 33 (1997): 40-46.

Gilman, Jeffrey W, Kashiwagi, T, Giannelis, EP, Manias, E, Lomakin, S, Lichtenhan, JD and Jones P. "Fire Retardancy of Polymer", M. Le Bras, G. Camino, S. Bourbigot, R. Delobel, Eds., The Royal Society of Chemistry, Cambridge, 1998.

Gilman, Jeffrey W, Kashiwagi, T. Polymer-Clay Nanocomposites; Pinnavaia TJ, Beall GW. Eds.; John

Wiley & Sons: New York, 2000, pp 193-205.

Gilman, Jeffrey W. "Flammability and Thermal Stability Studies of Polymer Layered-Silicate (Clay) Nanocomposites". Appl Clay Sci 15 (1999): 31–49.

Hirschler, MM and Shakir, S. Proceedings Flame Retardants. London: Elsevier Applied Science, 1992.

Kojima, Y, Usuki, A, Kawasumi, M, Okada, A, Fukushima, Y, Kurauchi, T and Kamigaito, O. "Mechanical properties of nylon 6-clay hybrid". J Mater Res 8 (1993): 1185–89.

Kojima, Yoshitsuqu, Usuki Arimitsu, Kawasumi, Masaya, Okada, Akane, Kurauchi, Toshio and Kamigaito, Osami"One-Pot Synthesis of Nylon 6–Clay Hybrid". J Polym Sci Part A: Polym Chem 31 (1993): 1755–58.

Kumar, Annamalai P, Depan, Dilip, Tomer, Namrata S and Singh Raj P. "Nanoscale Particles for Polymer Degradation and Stabilization—Trends and Future Perspectives". Prog Polym Sci 34 (2009): 479–515.

Le, BM, Camino, G, Bourbigot, S and Delobel, R. Fire Retardancy of Polymers: The Use of Intumescence. Royal Society of Chemistry: Cambridge, 1998, pp 196.

Lewin, Menachem. "Some comments on the modes of action of nanocomposites in the flame retardancy of polymers". Fire Mater 27 (2003): 1-7.

Liu, Pinggui, Gong, Kecheng, Xiao, Peng and Xiao, Min. "Preparation and characterization of poly(vinyl acetate)-intercalated graphite oxide nanocomposite". J Mater Chem 10 (2000): 933–935.

Liu, Ying-L, Hsu, Chih-Y and Hsu Keh-Y. "Poly (methylmethacrylate)-silica nanocomposites films from surface-functionalized silica nanoparticles". Polymer 46 (2005):1851–56.

Mouritz, AP, Mathys, Z and Gibson, AG. "Heat release of polymer composites in fire". Composites: Part A 37 (2006): 1040–54.

Peeterbroeck, S, Alexandre, M, Nagy, JB, Pirlot, C, Fonseca, A, Moreau, N, Pjilippin, G, Delhalle, J, Mekhalif , Z, Sporken, R, Beyer, G and Dubois, P. "Polymer-Layered Silicate-Carbon Nanotube Nanocomposites: Unique Nanofillers Synergistic Effect". Comp Sci Technol 64 (2004): 2317-23.

Porter D, Metcalfe E, Thomas MJK. "Nanocomposite Fire Retardants – A Review". Fire Mater 24 (2000): 45–52.

Preston, Christopher ML, Amarasinghe, Gandara, Hopewell, Jefferson L, Shanks, Robert A and Mathys Zenka. "Evaluation of Polar Ethylene Copolymers as Fire Retardant Nanocomposite Matrices". Polym Degrad Stab 84 (2004): 533–44.

Ray, Suprakash S, Okamoto, Kazuaki and Okamoto Masami. "Structure−Property Relationship in Biodegradable Poly (Butylene Succinate)/Layered Silicate Nanocomposites". Macromolecules 36 (2003): 2355–67.

Sahoo, Prafulla K, Mohapatra Rumki. "Synthesis and kinetic studies of PMMA nanoparticles by non-conventionally initiated emulsion polymerization". Euro Polym J 39 (2003): 1839–46.

Sahoo, Prafulla K, Samal, Ramakanta, Swain, Sarat K and Rana, Pradip K. "Synthesis of Poly (Butyl Acrylate)/Sodium Silicate Nanocomposite Fire Retardant". Euro Polym J 44 (2008): 3522–28.

Sahoo, Prafulla K and Samal, Ramakanta. "Fire Retardancy and Biodegradability of Poly (Methyl Methacrylate) /Montmorillonite Nanocomposite". Polym Degrad Stab 92 (2007):1700–7.

Samal, Ramakanta and Sahoo Prafulla K. "Synthesis of a Biodegradable Polyacrylonitrile/ Sodium Silicate Nanocomposite Fire Retardant". Indian J Chem Techn 17 (2010): 139-144.

Scudamore, MJ, Briggs, PJ and Prager FH. "Cone Calorimetry - A Review of Tests Carried Out on Plastics for the Association of Plastic Manufacturers in Europe". Fire Mater 2 (1991): 65-84.

Swain Sarat K and Isayev AI. "Effect of Ultrasound on HDPE/Clay Nanocomposites: Rheology Structure and Properties". Polymer 48 (2007): 281–89.

Warson H and Finch CA. Application of Synthetic Resin Latices. Wiley: New York, 2001.

Weil, Edward D, Patel, Navin G, Said, MM, Hirschler, Macrelo M, and Shakir, S. "Oxygen Index: Correlations to Other Fire Tests". Fire Mater 16 (1992): 159.

Zanetti, M, Kashiwagi, T, Falqui, L and Camino G. "Cone Calorimeter Combustion and Gasification Studies of Polymer Layered Silicate Nanocomposites". Chem Mater 14 (2002): 881–87.

Zhang, Xingui and Loo, Leslie S. "Synthesis and thermal oxidative degradation of a novel amorphous polyamide/nanoclay nanocomposite". Polymer 50 (2009): 2643.

International Journal of Material Science (IJMSCI) Volume 4 Issue 3, September 2014 www.ij-ms.org
doi: 10.14355/ijmsci.2014.0403.02

Severe Plastic Deformation Methods to Achieve Nanostructured Materials

Seyedhossein Miran

Department of Materials Science and Engineering, Friedrich Alexander University of Erlangen-Nürnberg
Martensstr. 5, 91058 Erlangen, Germany

seyedhossein.miran@studium.uni-erlangen.de

Abstract

Nanostructured materials possess interesting properties and the techniques for achieving them, have generated much interest in recent years. Severe Plastic Deformations (SPD) processes are among those techniques for generating bulk nanostructured materials; in this paper the major conventional SPD methods including High Pressure Torsion (HPT), Equal Channel Angular Pressing (ECAP), Accumulative Roll Bonding (ARB) and Constrained Groove Pressing (CGP) are reviewed. The most recent proposed SPD processes of Continuous High Pressure Torsion (CHPT) and Cone-Cone Method (CCM) are also presented. Finally, some applications of the SPD processed materials in the market are discussed.

Keywords

Severe Plastic Deformation (SPD); Nanostructured Materials; High Strength; Applications

Introduction

Severe Plastic Deformation (SPD) processes is defined as processes in which an ultra-large plastic strain is introduced into a bulk material in order to create ultra-fine grained structures [A. Azushima *et al.*, 2008]. Materials produced by SPD techniques usually have grain sizes in the range of 100-1000 nm, however they have subgrain structures, such as dislocation cells, subgrains and X-ray coherent diffraction domains (crystallites) which are often smaller than 100 nm. Therefore, they can be called nanostructured materials [Yuntian T. Zhu *et al.*, 2004].

In a simple tensile test in ductile materials, the imposed plastic strain is less than 1.0 and in the conventional metal forming processes such as rolling and forging, the strain is generally less than 2.0 but in SPD the strain could be as high as 4.0 [A. Azushima *et al.*, 2008].

The yield stress of metallic materials at room temperature increases with the decreasing grain size, which is known as the Hall-Petch relationship, is represented by the following equation

$$\sigma_{(yield)} = \sigma_o + K D^{(-1/2)} \quad (1)$$

Where σ_0 is friction stress and K is a constant value and D is the size of grain, the principle of SPD processes is exactly based on this equation.

All of the SPD processes work based on this idea that Bulk Nanostructured Materials (BNMs) have higher strength; over last decade the development of BNMs has become one of the most topical directions in modern materials science. The use of SPD techniques has attracted special attention, because these techniques provide new opportunities for developing different fabrication for various semi-products in the form of sheets, rods, thin foils and wires [R. Z. Valiev *et al.*, 2007].

Various aspects of structural changes caused by SPD have been the research goals in laboratories worldwide. Hundreds of papers are published each year in distinguished journals and conference proceedings. Today the most effort is paid to the study of the mechanics of material flow and grain subdivision when low strains ($\varepsilon_{ev} < 3.0$) and high strains ($\varepsilon_{ev} > 3.0$) are applied at SPD [J. Zrink *et al.*, 2008].

This review paper first highlights the main conventional SPD processes; then, some new SPD techniques will be discussed. Finally, the applications of the achieved nanostructured materials by SPD processes in industrial scale will be presented.

SPD Processes

There are different techniques to refine grains of materials (consolidation of ultra fine particles, electrodeposition, crystallization of amorphous, severe plastic deformation, thermomechanical controlled processes etc.); FIG. 1 illustrates respective resulted grain size for each method:

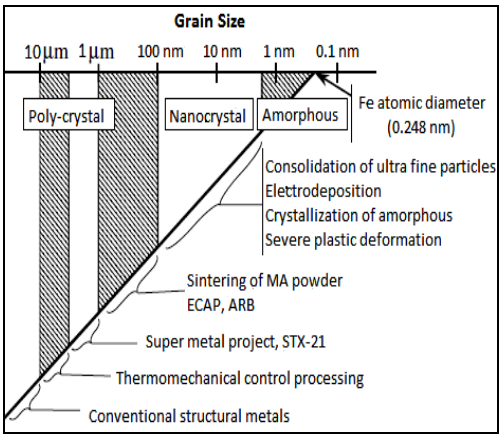

FIG. 1 PRODUCTION METHODS OF FINE GRAINED MATERIALS AND RESPECTIVE GRAIN SIZE RANGE [M. Umemoto, 2003]

High Pressure Torsion (HPT)

Severe plastic deformation by high pressure torsion involves the deformation of discs by pure shear between two anvils in which one anvil rotates against the other anvil holding the material. FIG. 2 shows schematically this process [R. Srinivasan *et al.*, 2006]:

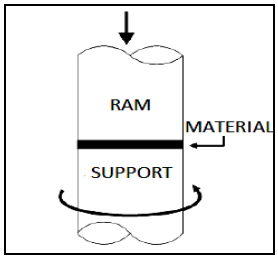

FIG. 2 HIGH PRESSURE TORSION PROCESS [R. Srinivasan *et al.*, 2006]

HPT was first investigated by Bridgman but his experiment did not bring much light on the microstructural changes taking place in severely deformed materials. It was Erbel who seemed to be the first carrying out HPT for copper. In HPT method a coin-shape sample is pressed between two anvils under hydrostatic pressure (~ 7 GPa) [J. Zrink *et al.*, 2008]. Moreover, the torque in this technique is provided by the punch via the contact friction at the sample/punch interface. The grain size of various metallic materials is refined to the submicrometer or nanometer ranges and consequently the HPT processing leads to the enhancement of strength and ductility. Second phase particles may be refined significantly and occasionally they are dissolved into the matrix. The HPT process is capable of offereing a wide range of materials including relatively hard and low ductile materials such as intermetallics and Mg alloys [K. Edalati *et al.*, 2009].

The strain in torsion is given by

$$\gamma(r) = 2\pi nr / l \qquad (2)$$

where r is the distance from axis of the disk sample, n the number of rotation and l the thickness of the sample as illustrated in FIG. 3:

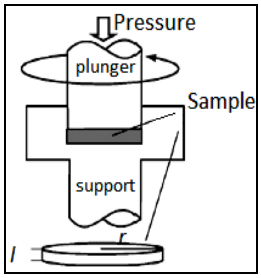

FIG. 3 DISC HPT PROCESS [A. Azushima *et al.*, 2008]

The equivalent strain according to the Von Mises yield criterion is given by [A. Azushima *et al.*, 2008]

$$\varepsilon(r) = \gamma(r) / \sqrt{3} \qquad (3)$$

Major limitation of HPT process is that the sample size is small typically as 10 mm in diameter with the thickness less than 1 mm and the microstructure develops inhomogeneously from the center to edge of the disk, because the generated strain according to equation (3) is proportional to the distance from the center [K. Edalati *et al.*, 2009]; however, detailed experiments on pure Ti and Ti-alloys demonstrated that HPT was the most effective SPD procedure for achieving grain refinement with reported average grain sizes of ~ 30 nm after HPT [Y. Harai et al., 2008].

Equal Channel Angular Pressing (ECAP) Process

ECAP is used for producing bulk ultra-fine grained materials; it was first developed by Segal (1977, 1995 and 1999). The main advantage of the process is that the work-piece can be subjected to uniform and high shear strain without major change in the shape and the size of work-piece. The general principle of ECAP is illustrated in FIG. 4:

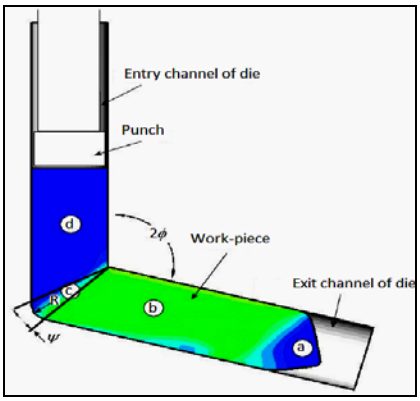

FIG. 4 SCHEMATIC OF ECAP PROCESS AND ZONES OF WORK-PIECE UNDER DEFORMATION (a) HEAD, (b) BODY, (c) PLASTIC DEFORMATION ZONE, (d) TAIL [B. V Patil *et al.*, 2008]

The work-piece is pressed through a die with channels

equal cross section, intersecting at an angle (channel angle, 2ϕ) ranging between 90° and 120°, having corner angle of ψ [B. V Patil *et al*., 2008]. In principle, if the fillet radius R is zero (sharp corner) the work piece will undergo simple shear as it passes through the plane of intersection between the two channels [R. Srinivasan *et al*., 2006].

Segal et al. (1995) have shown that theoretical equivalent plastic strain $\bar{\varepsilon_p}$ after n passes is given by [B. V Patil *et al*., 2008]

$$\bar{\varepsilon_p} = (2n / \sqrt{3}) \, . \, Cot\,(\phi) \quad (4)$$

ECAP has been applied to many materials, such as Al 6000 series alloys and steels [S. C. Yoon *et al*., 2010]. ECAP is also widely used to compact powders nearer to their theoretical density and to enhance the microstructure and mechanical properties of tubular materials. In recent years, various modifications to the ECAP processes, including rotary die ECAP, cross-ECAP and T-ECAP have been proposed. It has been found that the strain homogeneity of the ECAP process dictates the mechanical properties of deformed materials [A. V. Nagasekhar *et al*., 2010].

Accumulative Roll Bonding (ARB) Process

The ARB process consists in rolling a couple of overlapped sheets at a given temperature and thickness reduction ratio (e.g. 0.5). At suitable ARB conditions a bonding interface forms between sheets during the deformation process, due to temperature and plastic strain. The product of the first rolling cycle is cut in two similar sheets which are overlapped and rolled again by the same procedure as the first rolling cycle [S. Argentero, 2012].

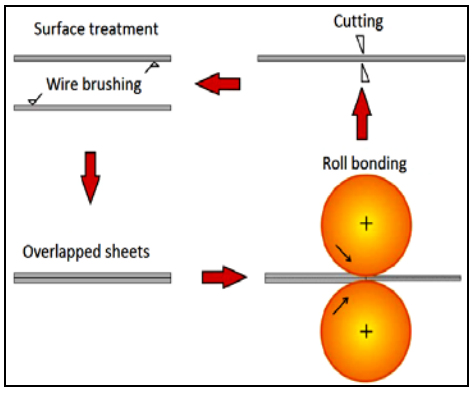

FIG. 5 ARB PROCESS [I. Topić, 2008]

ARB is a relative new SPD process, which was originally introduced and developed by Saito et al. in 1998. This process deforms plastically a metal slab or sheet by passing it between rolls which is known as rolling. During the process, the sheet is exposed to high compression stress due to squeezing action of the rolls and high surface shear stresses arising from friction between the sheet and the rolls [I. Topić, 2008]. FIG. 5 schematically shows the ARB process:

ARB process is a discontinuous process which keeps geometry and size of the billets constant; it is possible with ARB to obtain a reasonably homogenous microstructure and texture using small number of passes [G. Angella *et al*., 2010]. The strain in this process can be expressed by

$$\varepsilon = (\sqrt{3} / 2)\, ln\, r\,; \quad r = 1 - 2^{(-n)} \quad (5)$$

where n is the number of cycles and r is the reduction in thickness per cycle [A. Azushima *et al*., 2008].

ARB process, at this moment, is the most promising SPD process for the industrial production of bulky materials in the future. It has been clarified that the microstructure of the ARB processed Al is composed of so-called lamellar boundary structure similar to that in the heavily rolled Al. On the other hand, the microstructural evolution during the ARB process is much faster than in conventional cold-rolling (a big advantage of ARB process) [B. L. Li *et al*, 2006].

Constrained Groove Pressing (CGP) Process

In CGP process, the material is subjected to an intense plastic deformation through repeated dominant shearing and pressing (flattening) of plate. Unlike the widely used ECAP process for structure refinement, the CGP process has the advantage that large plastic deformation can be applied to the metal in sheet or plate form [J. Zrník *et al*., 2008]. CGP is a practical process to impose nearly uniform strain to specimen by asymmetrically grooved and flat dies [A. Sajadi *et al*., 2012].

In CGP process, a sheet is located between a pair of asymmetrically grooved dies; as the die presses the sheet, the inclined regions of the sheet are subjected to shear deformation under the plane-strain deformation condition ($\varepsilon_{eff} = 0.58$), then a pair of flat dies imposes a second pressing on the grooved sheet and a reverse shear deformation will be applied to grooved regions ($\varepsilon_{eff} = 1.16$) while the undeformed regions remain unchanged [A. Sajadi *et al*., 2012]. After this, the sheet will be rotated 180° to allow undeformed regions to be deformed exactly like the other deformed regions; in this way we may get a homogeneous strain of 1.16 in all the regions of the sheet.

FIG. 6 shows the six steps to reach the strain of 1.16 within the sheet:

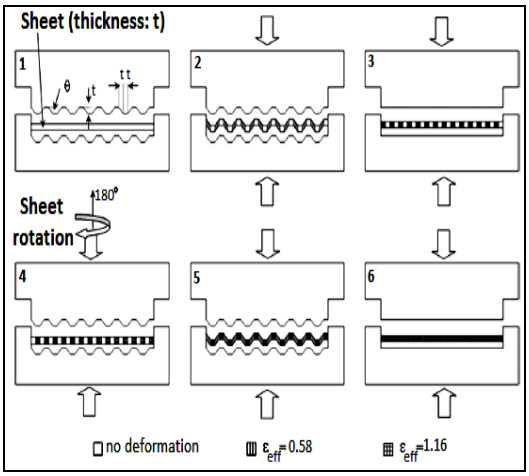

FIG. 6 SIX STEPS OF THE CGP PROCESS [E. Rafizadeh *et al.*, 2009]

The equivalent strain per these six steps is given by

$$\varepsilon = 4\, ln\, (\{(r + t) / (r + 0.5\, t)\} / \sqrt{3}) \qquad (6)$$

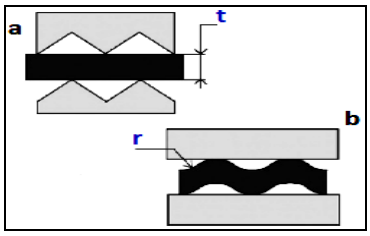

FIG. 7 PRINCIPLE OF REPETITIVE CORRUGATING AND STRAIGHTENING (CGP PROCESS) [A. Azushima *et al.*, 2008]

where t is the thickness of sheet and r is the curvature of bent zone (FIG. 7). By repeating these six steps, high strains can be introduced in the sheet [A. Azushima *et al.*, 2008].

New SPD Processes

Continuous High-pressure Torsion (CHPT) Process

High Pressure Torsion (HPT) introduced in above section, has three main limitations: first, the sample shape is in the form of disk which is not suitable for many industrial applications compared to wires and sheets. Second, the sample size is restricted to a maximum of 35 mm in diameter. Third, the generated strain is proportional to the distance from the disk center, so an inhomogeneous distribution of microstructure could be expected across the diameter. Therefore, a new alternative SPD process is developed for metallic sheets with HPT in a continuous manner, called Continuous High Pressure Torsion (CHPT) [K. Edalati *et al.*, 2010].

FIG. 8 illustrates CHPT process, there are two anvils (lower anvil is rotated during the process and upper anvil which is fixed and a U-shaped specimen is used as an initial sample):

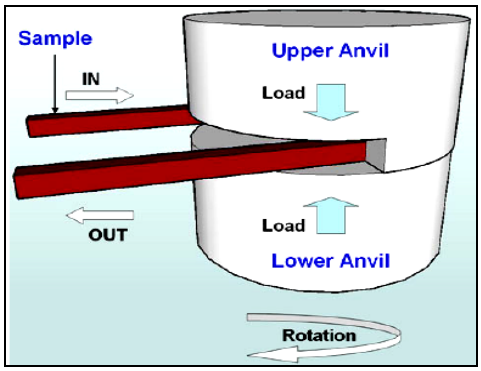

FIG. 8 CHPT PROCESS [K. Edalati *et al.*, 2010]

The equivalent strain produced by CHPT is given by

$$\varepsilon = (\{(1\text{-}s)\, \pi\, R\} / (t\, \sqrt{3})) \qquad (7)$$

where s is the fraction of sample slippage, R is the mean radius of U-shaped sample and t is the thickness of the specimen [K. Edalati *et al.*, 2010].

Sheets with high purity Al, Cu and Fe have been successfully processed with this technique with the result of enhanced hardness and microstructural refinement. FIG. 9 shows the U-shape specimen before and after deformation:

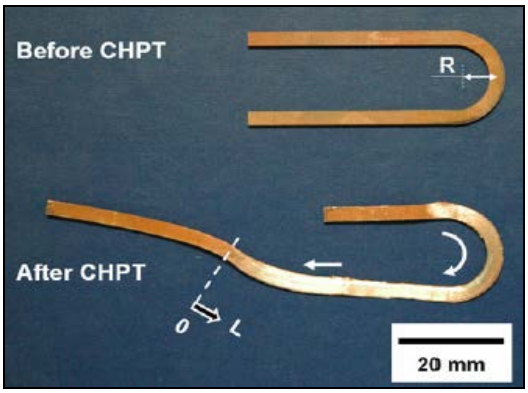

FIG. 9 U-SHAPE SPECIMEN BEFORE AND AFTER DEFORMATION [K. Edalati *et al.*, 2010]

Cone-Cone Method (CCM)

This SPD process is based on the use of a conical tool (plunger) and a conical die to deform a conical ring of a given material by applying a force F and a torque C on the tool (FIG. 10). The force is used to impose hydrostatic pressure and the torque is used to deform the ring by shear. By cutting the deformed workpiece and then rolling, flat products with fine grained structure could be obtained; In 2009, Bouaziz et al. reported the first results of numerical simulations of the CCM which demonstrated the feasibility of the process [O. Bouaziz *et al.*, 2009].

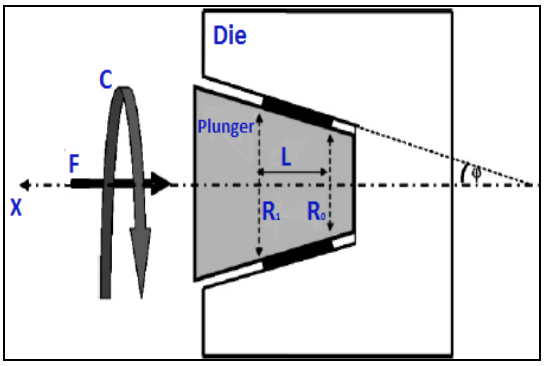

FIG. 10 CCM DESIGN, THE CONICAL SHEET SAMPLE (SHOWN IN BLACK) IS PLACED BETWEEN DIE AND PLUNGER [O. Bouaziz *et al.*, 2009]

In addition to CHPT and CCM, there are some other processes which can provide a large plastic deformation to have nanostructured materials.

Equal Channel Angular Extrusion (ECAE) with rotating tooling and Reversed Shear Spinning (RSS) are among these SPD processes (FIG. 11):

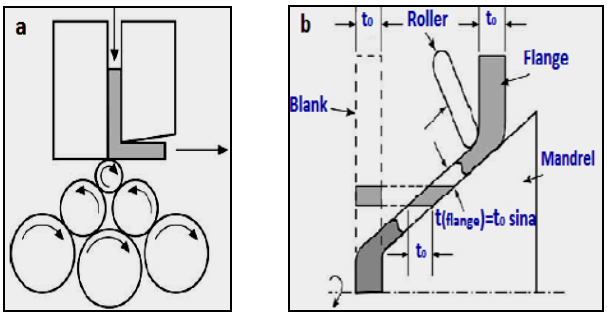

FIG. 11 TWO NEW SPD PROCESSES: (a) ECAE PROCESS, (b) RSS PROCESS [David J. Alexander, 2007]

Applications of SPD Processes

As it is expected from the products of SPD processes, they show both high strength and high ductility properties; these materials are top choice for the structural uses. The SPD processed materials have higher strength/weight ratio compared to conventional deformed materials, the SPD processes also keep the shape and dimensions of the workpiece the same as before the deformation. The two mentioned factors are significant advantages of SPD processes to be used in large scale of industrial applications.

Among the industrial applications of SPD techniques, bolts in the automobile and aircraft industries are manufactured with titanium alloys using ECAP process shown in FIG. 12:

One of the first commercial applications of bulk ultra-fine grained (UFG) metals is in sputtering targets for physical vapor deposition (PVD) out of Al and Cu up to 300 mm in diameter, produced from plates by ECAP. They are used for metallization of silicon wafers in semiconductors industries. An advantage of using UFG sputtering targets compared to coarse grained ones is that a more uniform deposited coating can be achieved which results from reduced arcing. The life span will also increase by 30% due to the stronger material.

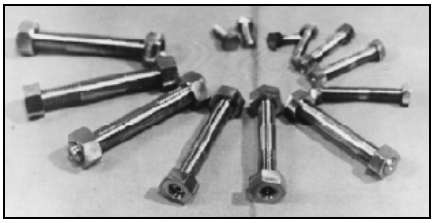

FIG. 12 HIGH STRENGTH BOLTS OUT OF Ti ALLOY USING ECAP PROCESS [A. Azushima *et al.*, 2008]

FIG. 13 shows a sputtering target from plates processed by ECAP [A. Azushima *et al.*, 2008]:

FIG. 13 SPUTTERING TARGET USING SPD METHOD [A. Azushima *et al.*, 2008]

Some other areas in which SPD processes could be beneficial are medical implants (nanostructured Ti as dental, hip and knee implants), defense industries (armor plates) and sport equipments (high strength metallic core of golf balls, airflow racquets as a composite of carbon fibers and nanocrystalline metal).

Conclusion

Different severe plastic deformation processes to achieve nanostructured materilas including main conventional techniques (HPT, ECAP, ARB and CGP) and two recent developed SPD methods (CHPT and CCM) in this paper have been reviewed.

There is no doubt that new SPD processes in near future will be proposed but a process will be commercially used which would produce nanostructured bulk materials with practically appropriate dimensions. It is also important to know the necessary post-treatment processes like heat treatment after SPD to get desired properties. The cost to convert the laboratory size to large scale applications is the next decisive factor for an

industrialized SPD process.

REFERENCES

A. Azushima, R. Kopp, A. Korhonen, D.Y. Yang, F. Micari, G.D. Lahoti, P. Groche, J. Yanagimoto, N. Tsuji, A. Rosochowski, A. Yanagida, "Severe plastic deformation (SPD) for metals." CIRP Annals – Manufacturing Technology, 2008. 57: p. 716-735.

A. Sajadi, F.J., M. Borhani, "Experimental and numerical investigation of groove pressed UFG pure aluminum." Advanced Design and Manufacturing Technology, 2012. 5 (2).

A. V. Nagasekhar, S.C.Y., J. H. Yoo, S.-Y. Kang, S. C. Baik, M. I. A. El Aal, H. S. Kim, "Plastic flow and strain homogeneity of an equal channel angular pressing process enhanced through forward extrusion." Materials Transactions, 2010. 51(5): p. 977-981.

B. L. Li, N. T., N. Kamikawa, "Microstructure homogeneity in various metallic materials heavily deformed by accumulative roll-bonding." Materials Science and Engineering A, 2006. 423: p. 331-342.

B. V Patil, U. Chakkingal, T S Prasanna Kumar, "Influence of friction in equal channel angular pressing – a study with simulation." Metal 2008, 2008.

David J. Alexander, "New methods for severe plastic deformation processing." Materials Engineering and Performance, 2007. 16(3): p. 360-374.

E. Rafizadeh, A.M., M. Kazeminezhad, "The effects of intermediate and post-annealing phenomena on the mechanical properties and microstructure of constrained groove pressed copper sheet." Materials Science and Engineering A, 2009. 515: p. 162–168.

G. Angella, D.D., S. Farè, M. Vedani, "A comparison between asymmetric rolling and accumulative roll bonding as means to refine the grain structure of an Al-Mg-Si alloy." Metallurgical Science and Technology, 2010. 28(1): p. 22-26.

I. Topić, "Ultrafine-grained metal sheets produced using the accumulative roll bonding process for light-weight structures." in der Technischen Fakultät der Universität Erlangen-Nürnberg, 2008.

J. Zrink, S. V. Dobatkin, I. Mamuzic, "Processing of metals by severe plastic deformation (SPD) – structure and mechanical properties respond." Metalurgija, 2008. 47 (3): p. 211-216.

J. Zrník, T. K., M. Cieslar, "CGP forming method to produce ultrafine grained structure in aluminum." METAL 2008.

K. Edalati, Z. Horita, "Scaling-up of high pressure torsion using ring shape." Materials Transactions, 2009. 50(1): p. 92-95.

K. Edalati, Z.H., "Continuous high-pressure torsion." Materials Science, 2010. 45: p. 4578–4582.

M. Umemoto, "Nanocrystallization of steels by severe plastic deformation." Materials Transactions, 2003. 44(10): p. 1900-1911.

O. Bouaziz, Y.E., H. S. Kim, "A new technique for severe plastic deformation: The Cone–Cone Method." Advanced Engineering Materials, 2009. 11(12): p. 982-985.

R. Srinivasan, P. K. Chaudhury, B. Cherukuri, Q. Han, D. Swenson, P. Gros, "Continuous severe plastic deformation processing of aluminum alloys." Wright State University, 2006.

R. Z. Valiev, M. J. Zehetbauer, Y. Estrin, H. Werner Höppel, Y. Ivanisenko, H. Hahn, G. Wilde, Hans J. Roven, X. Sauvage, T. G. Langdon, "The innovation potential of bulk nanostructured materials." Advanced Engineering Materials, 2007. 9: p. 527-533.

S. Argentero, "Accumulative roll bonding technology of aluminum alloys." METAL 2012.

S. C. Yoon, A.V.N., J. H. Yoo, M. I. Abd El Aal, M. Vaseghi and H. S. Kim, "Deformation characteristics evaluation of modified equal channel angular pressing processes." Materials Transactions, 2010. 51(1): p. 46-50.

Y. Harai, M. Kai, K. Kaneko, Z. Horita, T. G. Langdon, "Microstructural and mechanical characteristics of AZ61 magnesium alloy processed by high-pressure torsion." Materials Transactions, 2008. 49(1): p. 76-83.

Yuntian T. Zhu, Terry C. Lowe, Terence G. Langdon, "Performance and applications of nanostructured materials produced by severe plastic deformation." Scripta Materialia, 2004. 51: p. 825-830.

International Journal of Material Science (IJMSCI) Volume 4 Issue 3, September 2014 www.ij-ms.org
doi: 10.14355/ijmsci.2014.0403.03

Metal-induced Effect of Antimony Addition on Some Physico-chemical Properties of $Se_{80}Te_{20}$ Inorganic Glass

Shipra Saraswat*[1], S. D. Sharma[2]

Department of Chemistry, IFTM University, Moradabad, India

*[1]dr_shipra_saraswat@yahoo.com

Abstract

Chalcogenide glasses are well known advanced functional materials for widely use in phase change optical recording technology. The present papers reports our novel research work regarding the metal-induced effects of Sb on some significant physico-chemical properties (coordination number, constraints, density, molar volume, cohesive energy, heat of atomization etc) of binary $Se_{80}Te_{20}$ glass. Our results indicate that there is a strong correlation between the structural modifications and significant variation in various physico-chemical parameters of parent glassy alloy after inclusion of Sb.

Keywords

Chalcogenide Glasses; Compactness; Average Coordination Number; Mean Bond Energy

Introduction

Se and Te belonging to VI B group elements are efficient materials for thin film circuits, fabrication of semiconductor devices, transistors and detectors. The properties of amorphous Se (a-Se) and the effect of alloying Te into glassy Se have been studied by various workers. It has been found by various workers that the structure of glassy Se-Te system is considerably modified by addition of Sb. Studies on Se-Te-Sb system in chalcogenide glasses which have received attention in beginning because of their important applications as photoreceptors in xerography and in switching devices [Mehra, 1991; Elliot, 1991]. The X-Ray K-absorption studies in glassy $Se_{80}Te_{20}$ and $Se_{80}Te_{10}Sb_{10}$ have been reported by Agnihotri et al [Agnihotri, 1988]. Effect of incorporation of Sb on the photoconductivity of amorphous thin films of $Se_{80}Te_{20}$ has been studied by Tripathi and Kumar [Tripathi, 1988].

Composition dependence of photoconductivity in amorphous thin films of $Se_{70}Te_{30-x}Sb_x$ has been reported by Dwivedi et al [Dwivedi, 1993]. High-field conduction studies in amorphous thin films of $Se_{80-x}Te_{20}Sb_x$ have been studied by Kumar et al [Kumar, 1998].

Light induced thermal crystallization of amorphous $Se_{70}Te_{30-x}Sb_x$ has been reported by Agrahari et al [Agrahari, 1996]. They found that rate of crystallization increases under illumination but light has no considerable influence on activation energy of crystallization (E_c). Dielectric relaxation in glassy $Se_{80-x}Te_{20}Sb_x$ has been investigated by Goel et al [Goel, 1997].

Calorimetric studies on different contents of Sb in Se-Te-Sb glassy system have been reported by various workers [Abdel-Rahim, 1998; Maharajan, 2000; Tiwari, 2006; Moharram, 2002]. Their results show that kinetic parameters of glass transition and crystallization are considerably affected by the variation of Sb concentration in Se-Te-Sb system. The isothermal and non-isothermal crystallization of bulk $Se_{80-x}Te_{20}Sb_x$ ($0 \leq x \leq 15$) has been studied by Singh et al [Singh, 1999]. It has been concluded by them that the values of 'E_c' determined by both isothermal and non-isothermal crystallization data are in good agreement with each other.

The investigation of MN rule in thin films of $Se_{80-x}Te_{20}Sb_x$ for different phases (amorphous, partially crystalline and crystalline phases) has been studied by Mehta et al [Mehta, 2005]. Their results show that the pre-exponential factor (σ_0) and activation energy (ΔE) satisfies the MN rule for amorphous thin films of $Se_{80-x}Te_{20}Sb_x$. However, MN rule is not obeyed for the thin films of other two phases. The applicability of MN rule for the pre-exponential factor K_o of crystallization rate constant K and the activation energy of crystallization E_c in isothermal crystallization process of glassy $Se_{70-x}Te_{30}Sb_x$ and $Se_{85-x}Te_{15}Sb_x$ alloys is also reported by Mehta et al [Mehta, 2006; Mehta, 2008]. High field

conduction studies in a-$Se_{80-x}Te_{20}Sb_x$ thin films in dark as well as in presence of light have been reported by Kushwaha and Kumar [Kushwaha, 2004]. The results indicate that dominated mechanism of the conduction in these samples is of Pool-Frenkel type in dark as well as in presence of light.

From the above literature survey, one can see that various physical properties of Sb containing Se-Te system have been studied in details but no serious attempts have been done to estimate their physic-chemical properties, which is relatively less studied. This motivated us to work in tis untouched direction. In the present article, the various physico-chemical properties of ternary Se-Te-Sb system are studied.

This document is a template. An electronic copy can be downloaded from the journal website. For questions on paper guidelines, please contact the publications committee as indicated on the journal website. Information about final paper submission is available from the journal website.

Experimental

Glassy $Se_{80-x}Te_{20}Sb_x$ ($0 \le x \le 15$) alloys were prepared by the melt-quenching method. The exact proportions of high-purity (99.999%) elements, accordance with their wt. %, were weighed using an electronic balance with an accuracy of 10^{-4} gm. The materials were then sealed in evacuated (~ 10^{-6} Torr) quartz ampoules (length ~ 5 cm and internal diameter ~ 8 mm). The vacuum of 10^{-5} Torr was achieved using high-vacuum pumping system (HindHivac, Model: VS65D). A liquid-nitrogen trap was used to enhance the vacuum from 10^{-5} Torr to 10^{-6} Torr. The ampoules were placed inside a furnace and the temperature rose at a rate of 3-4 ^{o}C /min to 1000^{o}C. During heating, the ampoules were constantly rocked, by rotating a ceramic rod to which the ampoules were attached, in order to obtain homogeneous amorphous alloys. After rocking for about 12 h, the obtained melts were cooled rapidly by removing the ampoules from the furnace and dropping them into ice-cooled water. The ingots of the samples were then removed by breaking the quartz ampoules.

Results and Discussion

Topological Considerations

The structural changes in the host Se-Te glassy alloy with Sb concentration may be explained on the basis of coordination number of the system. For the glassy $Se_{80-x}Te_{20}Sb_x$ ($0 \le x \le 15$) alloys, the average coordination number $\langle r \rangle$ can be calculated using the formula:

$$\langle r \rangle = \frac{\alpha N_{Se} + \beta N_{Te} + \gamma N_{Sb}}{100} \quad (1)$$

Here α, β and γ are the atomic percentages of Se, Te and Sb and N_{Se}, N_{Te} and N_{Sb} are the coordination numbers of Se, Te and Ag respectively.

In covalent solids, there are two types of near-neighbor bonding forces; bond-stretching (α-forces) and bond bending (β-forces). The number of Lagrangian bond-stretching constraints per atom is $n_\alpha = \langle r \rangle/2$ and bond bending constraints is $n_\beta = 2\langle r \rangle - 3$. The total number of constraints (N_c) is sum of the bond bending and bond stretching constraints. The effective average coordination number $\langle r_{eff} \rangle$ can be calculated [Thorpe, 1983] using the formula;

$$\langle r_{eff} \rangle = \frac{2(N_C + 3)}{5} \quad (2)$$

TABLE 1 VALUES OF AVERAGE COORDINATION NUMBER ($\langle R \rangle$), BOND STRETCHING CONSTRAINTS (N_A), BOND BENDING CONSTRAINTS (N_B), TOTAL NUMBER OF CONSTRAINTS PER ATOM (N_C) AND FRACTION OF FLOPPY MODES (F) FOR GLASSY $SE_{80}TE_{20}$ AND $SE_{80-x}TE_{20}SB_x$ ($0 \leqslant x \leqslant 15$) ALLOYS

Sample	$\langle r \rangle$	n_α	n_β	n_c	f
$Se_{80}Te_{20}$	2.0	1	1	2	0.33
$Se_{75}Te_{20}Sb_5$	2.07	1.04	1.1	2.2	0.27
$Se_{70}Te_{20}Sb_{10}$	2.15	1.07	1.3	2.4	0.21
$Se_{65}Te_{20}Sb_{15}$	2.22	1.12	1.4	2.6	0.14

Thorpe estimated the number of constraints by using the Maxwell counting [Fadel, 1997], which is a procedure originally devised to determine the stability of a network of rods connected with pivot joints. In this counting, each coordinated atom is associated with bond-stretching constraints ($\langle r \rangle/2$) that come from the radial force, since there are r bonds, each of them are shared by two atoms. In each atom, there are ($2\langle r \rangle - 3$) bond bending constraints that come from the angular forces. Using this counting, the fraction of floppy modes with respect to the degree of freedom is:

$$f = 2 - \frac{5 < r >}{6} \quad (3)$$

The value of f approaches zero when $\langle r \rangle$ approaches the critical value of 2.4. Networks with $\langle r \rangle < 2.4$ are polymeric glasses (or floppy) in which the rigid regions are isolated. As $\langle r \rangle$ increases, the network goes through the transition at $\langle r \rangle = \langle r_c \rangle = 2.4$. At this $\langle r_c \rangle$, the rigidity percolates and the glass transforms to a rigid structure. This $\langle r_c \rangle$ value is referred to as the

rigidity percolation or mechanical threshold. Networks with <r> > 2.4 are amorphous solids (or rigid). The calculated values of n_α , n_β, N_c, and f of glassy $Se_{80-x}Te_{20}Sb_x$ ($0 \le x \le 15$) system are shown in Table 1.

Density, Molar Volume and Compactness

Density is a significant physical parameter and it is widely used as assess of rigidity of the system. It is also related to the average coordination number of the system. It can be evaluated by using formula [Sharma, 2009]:

$$\rho = \left(\sum m_i / d_i\right)^{-1} \quad (4)$$

Here m_i is the fraction of mass and d_i is the density of i^{th} structural unit.

TABLE 2 VALUES OF DENSITY (P), MOLAR VOLUME (V_M) AND COMPACTNESS (Δ) FOR GLASSY $SE_{80}TE_{20}$ AND $SE_{80-x}TE_{20}SB_x$ ($0 \leqslant X \leqslant 15$) ALLOYS

Sample	Density (g/cm³)	Volume (cm³/mol)	Compactness
$Se_{80}Te_{20}$	5.02	17.7	-0.022
$Se_{75}Te_{20}Sb_5$	5.13	17.8	-0.026
$Se_{70}Te_{20}Sb_{10}$	5.17	17.9	-0.029
$Se_{65}Te_{20}Sb_{15}$	5.25	18.1	-0.031

The density was measured hydrostatically in a medium of distilled water at a constant temperature. The values of density (ρ) are given in Table 2 for different glassy alloys. From this table it is clear that the density of ternary alloys is more than that of binary $Se_{80}Te_{20}$ alloy. In present system, Sb is incorporated in glassy $Se_{80}Te_{20}$ parent glass at cost of Se. Therefore, the observed results can be explained on the basis of the density of Sb and Se elements at room temperature. The density of Sb (~ 6.7 g cm^{-3}) is higher than that of Se (~ 4.8 g cm^{-3}). Therefore the higher density of chemical modifier Sb as compared to Se in present Se rich parent glass $Se_{80}Te_{20}$ is probably responsible for the increase in density of ternary alloys.

Using the value of density obtained from Eq. (4), the molar volume of the system is calculated by using the formula:

$$V_m = \frac{\sum x_i M_i}{\rho} \quad (5)$$

Here x_i represents the atomic fraction of i^{th} component and M_i is the corresponding atomic mass. The values of V_m are shown in Table 2 for individual glassy alloys.

From this table it is clear that the molar volume of ternary alloys is decreased with increase in Ag concentration in parent $Se_{80}Te_{20}$ glass. The atomic volume of Sb (~ 18.2 $cm^3\,mol^{-1}$) is also higher than that of Se (~ 16.5 $cm^3\,mol^{-1}$). Thus, the rise in molar volume of ternary alloys as compared to parent glass is evident after the incorporation of Sb as foreign atom. The variation of density and molar volume with average co-ordination number is shown in Fig. 1. From this figure, above mentioned facts are clearly revealed.

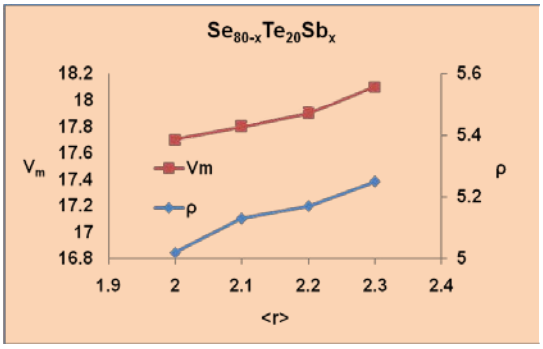

FIG. 1 VARIATION OF THE DENSITY AND MOLAR VOLUME, RESPECTIVELY, AS A FUNCTION OF AVERAGE CO-ORDINATION NUMBER <R> FOR GLASSY $Se_{80-x}Te_{20}Sb_x$ ($0 \le X \le 15$) ALLOYS.

The compactness (δ) was calculated by the formula [Savova, 1994; Tichy, 1994]:

$$\delta = \frac{\sum \frac{c_i A_i}{\rho_i} - \sum \frac{c_i A_i}{\rho}}{\sum \frac{c_i A_i}{\rho}} \quad (6)$$

Here C_i is the atomic fraction, A_i is the atomic weight; ϱ_i is the atomic density of the ith element of the glass. The calculated values of δ are listed in Table 2. The compactness is a measure of the normalized change of the mean atomic volume due to chemical interactions of the elements forming the network of a given solid [Skordeva, 1995]. Consequently, it is more sensitive to changes in the structure of the glass network as compared to the mean atomic volume.

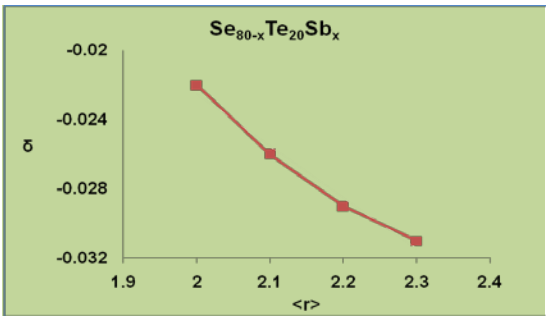

FIG. 2 PLOT OF COMPACTNESS VS AVERAGE CO-ORDINATION NUMBER FOR GLASSY $Se_{80-x}Te_{20}Sb_x$ ($0 \le X \le 15$) ALLOYS

The average coordination number dependence of the

compactness (δ) for the present glassy alloys is shown in Fig. 2. From this figure, it is evident that compactness is increased with increase in Sb concentration in parent $Se_{80}Te_{20}$ glass.

Lone Pair Electron

The lone-pair electrons (LP) are calculated using the relation:

$$LP = V - \langle r \rangle \quad (7)$$

Here *LP* is the number of lone-pair electrons, *V* is the valence electron which is equal to unshared lone-pair electron and $\langle r \rangle$ is the average coordination number. The evaluated values of L of glassy $Se_{80-x}Te_{20}Sb_x$ ($0 \leq x \leq 15$) system are tabulated in Table 2.

Zhenhua [Modgil, 2011] introduced a simple criterion for computing the ability of a chalcogenide system to retain its vitreous state; the criterion contains the number of lone-pair electrons which is necessary for obtaining the system in its vitreous state. For a binary system the number of lone-pair electrons must be larger than 2.6 and for a ternary system it must be larger than 1. This is clear from the Table 2 that the system under study is a good glass former. For a large number of lone-pair electrons the strain energy in a system decreases and thus structures with large numbers of lone-pair electron favor glass formation.

Parameter R and Mean Bond Energy

The Parameter R, deviation of stoichiometry, is expressed by the ratio of covalent bonding possibilities of chalcogen atom to that of non-chalcogen atom. For glassy $Se_{80-x}Te_{20}Sb_x$ ($0 \leq x \leq 15$) alloys, the quantity R is defined by [Tichy, 1995]:

$$R = \frac{\alpha N_{Se} + \beta N_{Te}}{\gamma N_{Sb}} \quad (8)$$

Here α, β and γ are the atomic fractions of Se, Te and Ag and N_{Se}, N_{Te} and N_{Sb} are the coordination number of Se, Te and Sb. There are three conditions arise for analysis of the parameter *R*.

(i) $R = 1$ indicates the stoichiometric composition, consisting only hetropolar bonds.

(ii) $R > 1$ symbolize the system is chalcogen rich and there are hetropolar bonds and chalcogen-chalcogen bonds exist.

(iii) $R < 1$ represent the system is selenium poor, hence hetropolar and metel-metel bonds formed.

For present investigating system the values of *R* are greater than 1 (see Table 3) leading the system to chalcogen rich region.

TABLE 3 PARAMETER (*R*), LONE PAIR ELECTRON (*LP*) AND OVERALL MEAN BOND ENERGY (<*E*>) FOR GLASSY $SE_{80}TE_{20}$ AND GLASSY $SE_{80-x}TE_{20}SB_x$ ($0 \leqslant x \leqslant 15$) ALLOYS

Sample	R	*LP*	Mean Bond Energy <E> (kcal/mol)
$Se_{80}Te_{20}$	∞	4.0	56.9
$Se_{75}Te_{20}Sb_5$	10.8	3.9	59.9
$Se_{70}Te_{20}Sb_{10}$	5.1	3.7	62.2
$Se_{65}Te_{20}Sb_{15}$	3.2	3.6	63.0

Tichy and Ticha [Zhenhua, 1991] were the first to point out that the value of glass transition temperature should not be only related to connectedness of the network (average coordination number $\langle r \rangle$) but should also be related to the quantity of connections, i.e. the mean bond energy between the atoms of the network. Since the difference in the bond energies of hetero-polar and homo-polar bonds is substantial [Sharma, 2007], so chemically ordered networks are expected where the number of hetero-polar bonds is maximized i.e. they are more favorably formed than homo-polar bonds. Since bulk glasses are considered, a chemical bond ordering model is assumed.

The bond energies (E_{AB}) of hetero-polar A-B bonds can be, in first approximation, estimated using Pauling's relation [Pauling, 1960]:

$$E_{AB} = 0.5\,(E_{A\text{-}A} + E_{B\text{-}B}) + 23\,(\chi_A - \chi_B)^2 \quad (9)$$

Here $E_{A\text{-}A}$ and $E_{B\text{-}B}$, and χ_A and χ_B are the, respectively, homo-polar bond energies and electro-negativities. The values of these physical quantities are obtained from [Weasr, 1979].

The degree of cross-linking per atom for chalcogen-rich region, as in the present case, can be expressed as:

$$P_r = \frac{aN_{Te} + bN_{Sb}}{(a + b + c)} \quad (10)$$

Here a, b and c are the ratio of atomic percentage of Te, Sb and Se respectively.

The mean bond energy of average cross-linking per atom (E_c) is given by:

$$E_c = P_r \,.\, E_{hb} \quad (11)$$

Here the average hetero-polar bond energy is given by:

$$P_{Eb} = \frac{aN_{Te}(E_{Se-Te}) + bN_{Ag}(E_{Se-Sb})}{(aN_{Te} + bN_{Sb})} \quad (12)$$

Here $E_{Te\text{-}Se}$ and $E_{Se\text{-}Sb}$ are the hetro-polar bond energies of Te-Se and Sb-Se hetero-polar bonds. The average bond energy per atom of the 'remaining matrix', E_{rm} is

defined as:

$$E_{rm} = \frac{2(0.5 < r > -P_r)(E_{Se-Se})}{< r >} \quad (13)$$

In equation (14) E_{Se-Se} is the homo-polar bond energy of the Se-Se bond in chalcogen-rich region.

Finally, the overall mean bond energy is given by

$$<E> = E_c + E_{rm} \quad (14)$$

The values of the overall mean bond energy for the glassy $Se_{80-x}Te_{20}Sb_x$ ($0 \le x \le 15$) alloys are given in Table 3. From the table it is clear that order of mean bond energy is increased with rise in Sb content in parent $Se_{80}Te_{20}$ alloy.

The plots of lone pair of electron (LP) and over all mean bond energy (<*E*>) against average co-ordination number are shown in Fig. 3 for glassy $Se_{80-x}Te_{20}Sb_x$ ($0 \le x \le 15$) alloys. From these plots, it is clear the number of lone pair electron (LP) decreases while increases in overall mean bond energy on the bonded atom. This is due to the electrostatics repulsion of lone pair of electrons of the two bonded atoms. This is probably the reason why LP is decreased but increase in <*E*>.

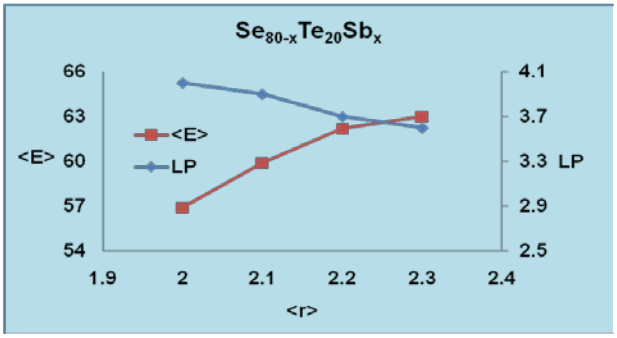

FIG. 3 VARIATION OF THE LONE PAIR ELECTRON AND MEAN BOND ENERGY, RESPECTIVELY, AS A FUNCTION OF AVERAGE CO-ORDINATION NUMBER <R> FOR GLASSY $SE_{80}TE_{20}$ AND GLASSY $Se_{80-x}Te_{20}Sb_x$ ($0 \le X \le 15$) ALLOYS

Cohesive Energy and Average Heat of Atomization

The cohesive energy (CE) of the system is the measure of the strength of a chemical bond and is defined as the stabilization energy of an infinitely large cluster of material per atom which allows determination of the number of possible bonds. According to the Zachariasen [Zacharisen, 1932] assumption, which is generally found to be valid for glass structure, atoms combine more favorably with atoms of different kinds than with the same kind. The condition is equivalent to assuming the maximum amount of chemical ordering possible. It favors the formation of an ageless structure by increasing the glass transition temperature T_g. Considering this assumption, bonds between like atoms will only occur if there is an excess of a certain type of atoms. Bonds are formed in the sequence of decreasing bond energies until all the available valences for the atoms are saturated. So according to this model the bond energies are assumed to be additive. Thus, the cohesive energy is calculated by summing the bond energies over all bond expected in the alloy:

$$CE = \sum \frac{C_i D_i}{100} \quad (15)$$

Where the C_i and D_i are the bond probabilities and D_i is the corresponding bond energy of the occurring bond in the glassy system. After all these bonds are formed, there are still unsatisfied Se valences "excess bonds" which must be satisfied by the formation of Se-Se bonds. The CE and numbers of excess bonds of glassy $Se_{80-x}Te_{20}Sb_x$ ($0 \le x \le 15$) alloys are listed in Table 4. Both the parameter (CE and number of excess bonds) exhibit the increasing trend in parent binary glass system with rise in Sb concentration. The plot of *CE* versus average co-ordination number <r> is shown in Fig. 4.

TABLE 4 COHESIVE ENERGY (CE), EXCESS SE-SE BOND AND AVERAGE HEAT OF ATOMIZATION ($\overline{H_s}$) OF GLASSY $SE_{80}TE_{20}$ AND GLASSY $SE_{80-x}TE_{20}SB_x$ ($0 \leqslant X \leqslant 15$) ALLOYS

Sample	Cohesive Energy (CE) (kcal/mol)	Excess Se-Se bond	Heat of Atomization ($\bar{H}_s$) (kcal/g-atom)
$Se_{80}Te_{20}$	56.9	120	48.7
$Se_{75}Te_{20}Sb_5$	58.0	92.5	49.4
$Se_{70}Te_{20}Sb_{10}$	59.2	65.0	50.0
$Se_{65}Te_{20}Sb_{15}$	60.6	37.5	50.6

From the data it is clear that the cohesive energy increases after the incorporation of Sb in parent glass at the cost of Se. The increase in the cohesive energy is due to the increases in the Se-Sb bonds and decreases in the Se-Se and Se-Te bonds. The bond energies of Se-Se and Se-Te bonds are less as compare to the Se-Sb bond energy. This is probably the reason why CE of ternary glasses is more than that of binary glass.

According to Pauling [Pauling, 1960], the heat of atomization H_s (A-B) at standard temperature and pressure of a binary semiconductor formed from A and B is the sum of heat of formation (ΔH) and the average heats of atomization (H_S^A) and (H_S^B), respectively, that corresponds to the average non-polar bond energy of the two atoms:

$$H_S(A-B) = \Delta H + 0.5(H_S^A + H_S^B) \quad (16)$$

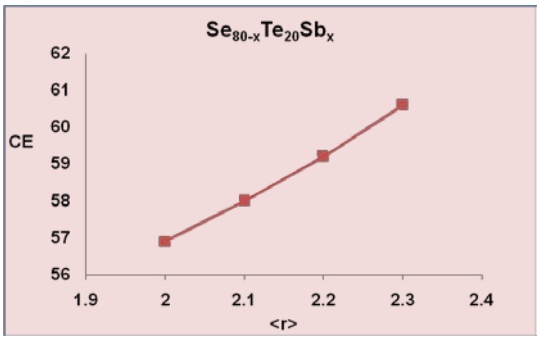

FIG. 4 PLOT OF COHESIVE ENERGY VS AVERAGE CO-ORDINATION NUMBER FOR GLASSY $Se_{80-x}Te_{20}Sb_x$ $(0 \le X \le 15)$ ALLOYS

The term (ΔH) in above equation is proportional to the difference between the electronegativities χ_A and χ_B of the two atoms:

$$\Delta H \propto (\chi_A - \chi_B)^2 \qquad (17)$$

In order to extend this idea to ternary and higher order semiconductor compounds [Sadagopan, 1965], the average heat atomization $\overline{H_s}$ (kcal/g atom) is defined for a compound $A_\alpha B_\beta C_\gamma$ as a direct measure of the cohesive energy and thus of average bond strength, given by

$$\bar{H}_S = \frac{(\alpha H_S^{Se} + \beta H_S^{Te} + \gamma H_S^{M})}{(\alpha + \beta + \gamma)} \qquad (18)$$

Here α β and γ are the ratios of Se, Te and foreign atom M (here M = Sb) respectively. H_S^{Se}, H_S^{Te}, and H_S^{M} are the heat of atomization of atoms Se, Te and M (M = Sb) respectively. The plot of $\bar{H}_S$ versus average co-ordination number <r> is shown in Fig. 5.

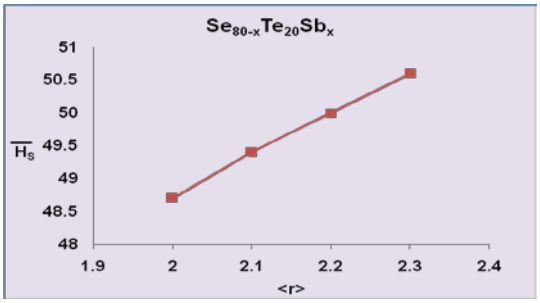

FIG. 5 PLOT OF AVERAGE HEAT OF ATOMIZATION VS AVERAGE CO-ORDINATION NUMBER FOR GLASSY $Se_{80-x}Te_{20}Sb_x$ $(0 \le X \le 15)$ ALLOYS

The values of $\bar{H}_S$ for different alloys are given in Table 4. It is interesting to note that the value of $\bar{H}_S$ of binary $Se_{80}Te_{20}$ alloy is also increased after the incorporation of Sb. This can be explained in terms of heat of atomization of Se, and Sb elements. In the present case, the chemical modifier Ag element is incorporated in binary $Se_{80}Te_{20}$ alloy at cost of Se. The heat of atomization of Se (~ 54.0 kcal mol^{-1}) is less than that of Sb (~ 62.3 kcal mol^{-1}). This is the probable reason of observed changes in the average heat of atomization of present alloys.

The structure of g-Se [Schotmiller , 1970; Lucovsky , 1967; Lucovsky, 1969] and the effect of alloying Te into g-Se [Das, 1972; El-Mously' 1978] have been studied by various workers. Their results have shown that ag-Se contains long polymeric chains and rings and have eight members in various proportions as its structural units, which are dissociated by the addition of Te in g-Se. The significant change in the various physico-chemical properties of glassy $Se_{80}Te_{20}$ alloy after incorporation of Sb can be explained to some extent with the help of Chemical ordered network model (CONM). According to CONM, the formation of hetero-polar bonds is favored over homo-polar bonds in glassy alloys. In Se-Te-M system, the various bonds involved are Se-Se, Te-Te, Se-Te, M-Se, M-Te etc. Addition of Sb as chemical modifier reduces Se-Se and Se-Te by making Se-Sb and Te-Sb bonds. The strength of Se-Se bond is greater than that of Te-Te bonds. The electro-negativity of Se is also greater than that of Te. Thus according to Pauling [Pauling, 1960], M-Se bonds are found stronger than M-Te bonds. Hence, the metallic additive (here Sb) is expected to combine preferably with Se. In past, Shukla et al [Shukla, 1989] also observed the same experimental fact in glassy $Se_{80}Te_{10}M_{10}$ alloys by using x-ray spectroscopy as a tool. Thus, our present results are in consistent with the results of Shukla et al [Shukla, 1989].

Conclusions

The physical behavior of glassy $Se_{80-x}Te_{20}Sb_x$ $(0 \le x \le 15)$ is investigated systemically as a function of average coordination number <r>. Our results indicate that there is a significant change in the structural environment of the parent glassy system due to rigidity percolation.

We have theoretically shown that our glassy samples are flexible (also referred as floppy or under-coordinated with <r> < 2.4 and $n_c < 3$. Antimony makes cross-linked structure with Se-Te chains and Se-Te mixed rings after entering in the glass matrix of parent glasses. The structure, therefore, becomes a new variable and various properties are affected due to structural rearrangements with increase in Sb concentration. The values of density and molar volume are found affected significantly after the incorporation of Sb in binary $Se_{80}Te_{20}$ alloy. This is

explained in terms of density of elements Se and Sb. The values of lone pair electron and parameter R show that present glasses are the members of chalcogen rich glassy system. The increasing sequence of average heat of atomization of ternary alloys depends on the heat of atomization of chemical modifier.

REFERENCES

Abdel-Rahim M. A., A study of the crystallization kinetics of some Se–Te–Sb glasses, J. Non-Cryst. Solids, 1998, Vol. 241, 121-127.

Agnihotri A. K., Kumar A., Nigam A. N., The X-ray K-absorption studies in glassy $Se_{80}Te_{20}$ and $Se_{80}Te_{10}Sb_{10}$ J. Non-Cryst. Solids, 1988, Vol. 101, 127-129.

Agrahari S. K., Dwivedi P. K., Kumar A., Light-induced thermal crystallization of amorphous $Se_{70}Te_{30-x}Sb_x$, Physica B, Vol. 1996, 226, 345-350

Das G. C., Bever M. B., Uhlmann D. R., Relaxation phenomena in amorphous selenium-tellurium alloys, J. Non-cryst. Sol., 1972, Vol. 7, 251-270 .

Dwivedi P. K., Srivastava S. K., Kumar A., Composition dependence of photoconductivity in amorphous thin films of $Se_{70}Te_{30-x}Sb_x$, IL Nuovo Cimento, 1993, Vol. 15, 1149-1157.

Elliot S. R., 1991 "Materials Science and Technology" (VCH Publisher Inc. New York) vol. 9 p. 446.

El-Mously M. K., El-Zaidia M. M., Thermal and electrical conductivities during the devitrification of $TeSe_{12.5}$ amorphous alloy, J. Non-cryst. Sol., 1978, Vol. 27, 265-271.

Fadel M., The physical properties and the chemical bond approach for Se-Ge-As amorphous chalcogenide glasses, Vacuum, 1997, Vol. 48, 73-83.

Goel D. K., Singh C. P., Kumar A., Dielectric relaxation in glassy $Se_{80-x}Te_{20}Sb_x$, IL Nuovo Cimento, 1997, Vol. 19, 705-714.

Kumar A., Dixit M., Dwivedi S. K., Shukla R. K., Photoconductivity and high-field conduction studies in amorphous this films of $Se_{80-x}Te_{20}Sb_x$, IL Nuovo Cimento, 1998, Vol. 20, 1391-1404.

Kushwaha V. S., Kumar A., High field conduction studies in a-$Se_{80-x}Te_{20}Sb_x$ this films in dark as well as in presence of light, J. Optoelectron. Adv. Mater., 2004, Vol. 6, 1159-1165.

Lucovsky G., Comments on the structure of chalcogenide glasses from infrared spectroscopy. Mater. Res. Bull., 1969, Vol. 4, 505-514

Lucovsky G., Mooradian A., Taylor W., Wright G. B., Keezer R.C., Identification of the fundamental vibrational modes of trigonal, α-monoclinic and amorphous selenium, Sol. Stat. Commun., 1967, Vol. 5, 113-117.

Maharajan N. B., Bhadari D., Saxena N. S., Paudyal D. D., Husain M., Kinetic Studies of Bulk $Se_{85-x}Te_{15}Sb_x$ Glasses with x = 0, 2, 4, 6, 8 and 10, Phys. Stat. Sol. (a), 2000, Vol. 178, 663-670.

Mehta N., Kumar A., Applicability of Meyer-Neldel Rule for isothermal crystallization in glassy $Se_{70}Te_{30-x}Sb_x$ alloys, Materials Letters, 2006, 60, 725-729.

Mehta N., Kumar D., Kumar A., Investigation of Meyer-Neldel rule in thin films of $Se_{80-x}Te_{20}Sb_x$ for different states J. Phys. Studies, 2005, Vol. 8, 238-242.

Mehta N., Singh K., Pre-exponential factor for the non-isothermal crystallization in glassy $Se_{85-x}Te_{15}Sb_x$ ($0 \le x \le 10$) alloys, Philosophical Magazine, 2008, Vol. 88, 1411-1421.

Mehra R. M., Kaur G., Mathur P. C., Crystallization kinetics of bulk amorphous $Se_{80-x}Sb_xTe_{20}$, J. Mater. Sci., 1991, Vol. 26, 3433-3437.

Modgil V., Rangra V. S., The Study of the Theoretical Parameters of Ge Sn Substituted Pb Based Quaternary Chalcogenide Glasses at Their Rigidity Percolation Threshold, J. Optoelectron. Adv. Mater., 2011, Vol. 13, 158-164.

Moharram A. H., Abu-Sehly A. A., Abu El-Oyoun M., Soltan A. S., Physica B, 2002, Vol. 324, 344-351.

Pauling L., The nature of the Chemical Bond. 3rd ed., 1960, Cornell University Press, Ithaca, NY.

Sadagopan V., Gotos H. C., On the relationship of semiconductor compound properties and the average heats of atomization, Sol. Stat. Electron., 1965, Vol. 8, 529-534.

Savova E., Skordeva E., Vateva E., The topological phase transition in some Ge-Sb-S glasses and thin films, J. Phys. Chem. Sol., 1994, Vol. 55, 575-578

Schotmiller J., Tabak M., Lucovsky G., Ward A., The effects of valency on transport properties in vitreous binary alloys of selenium, J. Non-cryst. Sol., 1970, Vol. 4, 80-96.

Sharma A., Barman P. B., Effect of Bi incorporation on the glass transition kinetics of $Se_{85}Te_{15}$ glassy alloy, J. Therm. Anal. Calor., 2009, Vol. 96, 413-417.

Sharma P., Katyal S.C., Theoretical calculation of physical parameters of $Ge_{10}Se_{90-x}Te_x$ glassy alloys, J. Optoelectron. Adv. Mater., 2007, Vol. 9, 1994-1999.

Shukla R. K, Swarup S., Kumar A., Nigam A., X-ray K-absorption studies in glassy $Se_{80}Te_{20}$ and $Se_{80}Te_{10}M_{10}$ (M = Ag, Cd, In and Sb), Semicond. Sci. Tech., 1989, Vol. 4, 681-684.

Singh A., Kumar A., Nagpal A. K., Crystallizations kinetics in $Se_{80-x}Te_{20}Sb_x$ glassy alloys, Adv. Mater. Opt. Electron., 1999, Vol. 92, 95-106.

Skordeva E., Arsova D., A topological phase transition in ternary chalcogenide films, J. Non-Cryst. Sol., 1995, Vol. 192-193, 665-668.

Thorpe M. F., Continuous Deformation in Random Network, J. Non-cryst. Sol., 1983. 57, 355-370.

Tichy L., Ticha H., Covalent bond approach to the glass-transition temperature of chalcogenide glasses, J. Non-cryst. Sol., 1995, Vol. 189, 141-146.

Tichy L., Ticha H., On the chemical threshold in chalcogenide glasses. Mater. Lett., 1994, 21, 313-319.

Tiwari R. S., Mehta N., Agarwal P., Kumar A., Investigation of Antimony addition on the glass transition kinetics of $Se_{80}Te_{20-x}Sb_x$ using calorimetric measurements, Indian J. Phys., 2006, Vol. 80, 49-53.

Tripathi S. K., Kumar A., Effect of incorporation of Sb and Ge on the photoconductivity of amorphous thin films of $Se_{80}Te_{20,}$ J. Non-Cryt. Solids, 1988, Vol. 104, 229-236.

Weasr R. C., CRC Handbook of Chemistry and Physics, sixtieth ed. CRC Press, 1979, Boca Raton, FL.

Zacharisen W. H., The atomic arrangemnts in glasses, J. Am. Chem. Soc., 1932, Vol. 54, 3841-3851.

Zhenhua L., 1991. Chemical bond approach to the chalcogenide glass forming tendency, J. Non-cryst. Sol., 1991, Vol. 127, 298-305.

Shipra Saraswat was born in 1980 in Bulandshar, India. She She obtained her M.Sc. degree in Chemistry from Dr. B. R. Ambedkar University, India in 2002. She is actively engaged in area of Materials Chemistry from 2008.

At present, she is pursuing Ph.D. in Chemistry from IFTM University, India. She is investigating the metal-induced effects of different metals on the binary alloys of Selenium rich chalcogenide glasses. She has published various research papers in journals of international repute.

International Journal of Material Science (IJMSCI) Volume 4 Issue 3, September 2014 www.ij-ms.org
doi: 10.14355/ijmsci.2014.0403.04

The Improvement in Physical and Static Bending Properties of Woven Oil Palm Plywood

Norul Hisham Hamid[1], Mohd Fitri Yazid[1], Micheal David Hale[2]

[1]Department of Forest Production, Faculty of Forestry, University Putra of Malaysia, 43400, UPM Serdang, Selangor, Malaysia

[2]School of Environment, Natural Resources and Geography, Bangor University, Gwyned, LL57 2UW, United Kingdom

h_noroul@putra.upm.edu.my; m.d.hale@bangor.ac.uk

Abstract

The physical and static bending properties of woven oil palm plywood pre-treated with low molecular weight of phenol formaldehyde (LMWPF) were investigated using MS standard 1787: Part 6 and 10. The oil palm veneers were cut into three different split widths of 15, 20 and 25 mm; and manually woven into veneer sized of 40 cm^2. The plywoods were fabricated into three different matrix layers of Type 1 (all three layer contained woven veneers), Type 2 (only core layer contained woven veneer) and Type 3 (face and back layers contained woven veneer). All plywood were made using a urea formaldehyde resin (UF) with spread rate of 200g/m^2, pre-pressed for two minutes and hot pressed at 130 ˚C for 12 minutes. The results revealed that Type 1 plywood gave the lowest thickness swelling, while Type 3 gave the highest static bending properties.

Keywords

Oil Palm; Pplywood; Woven; Tthickness Swelling; Bending

Introduction

Many Malaysia wood-based industries especially plywood have concerned about the future supply of raw material, as indicates by closing down a number of factory. This is due to shrinkage of total production forest area, which aims to conserve more logged forest area.

Wood based industries are trying to find a good alternative source of raw materials, and oil palm biomass was currently appeared as the most viable alternative (Mohamad *et al.* 2005). Malaysia produced about 21.63 million cubic meters of oil palm biomass, including trunks, fronds, and empty fruit bunches. The total oil palm plantation area in Malaysia was expanded from merely 1.7 million hectares in 1990 to 4.8 million hectares in 2013; and Malaysia goverment is targeting for 5.8 million hectares of oil palm plantation by 2020. The annual availability of oil palm stem was estimated to be around 13.6 million logs based on 100 000 hectares of replanting each year (Anis et al. 2011).

The oil palm trunk had many weakness such as low strength, durability, dimensional stability, and machining properties (Anis et al., 2011). Conversion of low quality oil palm trunk into composites is a priority solution and its development was reported in a few studies (Rozman et al., 1997; Jacob et al., 2004; Abdul Khalil et al., 2010a; Abdul Khalil et al., 2010b; Hashim et al., 2010; Hashim et al., 2011; Mat Rasat et al., 2011; Abdullah et al., 2012). Among them, only oil palm plywood was successfully commercialised. The oil palm veneer found to be only suitable as a core layer integrated with a face and back layers of tropical hardwood veneer; due to its soft structure.

Approcah to overcome this weakness, Loh *et al.* (2010) impregnated the oil palm veneer with a low molecular weight phenol formaldehyde resin. The treatment of oil palm stem (OPS) veneers with low molecule weight of phenol formaldehyde (LMWPF) resin significantly improved the density, stiffness and bond integrity of oil palm plywood. The effects were more significant on the outer layer veneers of OPS; and the treatment was able to improve the modulus of rupture (MoR) by 115%, modulus of elasticity (MoE) by 70%, wet and dry shear strengths by 134% and 197% respectively. Adhesive spread amount did not significantly effect on the strength and bond integrity of OPS plywood except on MOE. Overall, the effect was only significant for outer veneers where an adhesive amount of 200 g/m2 was sufficient to produce good performance plywood.

The lower properties of LMWPF modified veneer from the inner OPS needs to be further improved for higher log recovery efficiency. This study aims to evaluate the physical and mechanical properties of woven oil palm plywood.

Materials and Method

Source of Materials

The veneers from inner portion of OPS were obtained from IK Panel (M) Sdn. Bhd. in Nibong Tebal, Penang, Malaysia. They were dried to 7- 9 % moisture content using a conventional kiln dry. The veneers of 5 to 6 mm thick were cut into 40 cm^2. The splits sized of 15, 20 and 25 mm (width) were cut using a circular saw and were manually woven with hand (Figure 1).

FIGURE 1. THE WOVEN OIL PALM VENEER.

Pre-treatment and Fabrication

The woven veneers were ballast with a metal rod wrapped with aluminium foil in tank contained low molecular weight phenol formaldehyde (LMWP, Table 1) for 2 hours. The submerged woven veneers were weighed to two decimal places; oven dried at 60 °C for 24 hours and its final weight was re-measured. The veneers were assembled into three plywood matrix as shown in Table 2. A single layer of urea formaldehyde resin (UF) with spread rate of 200g/m^2 was applied to veneer and pre-pressed for two minutes. The veneers were then hot pressed at 130 °C using a pressure of 100 bar for 12 minutes.

TABLE 1 THE PROPERTIES OF LMWP AND UF RESINS.

Properties	LMWP	UF
pH (at 30 °C)	8.48	8.74
Viscosity (at 30 °C)	0.07 poise	2.22 poise
Specific gravity (at 30 °C)	1.123	1.280
Solid content	30.1	65.3
Gel time (at 140 °C)	6 min	53 min

TABLE 2. THE TYPES OF PLYWOOD MATRIX.

Plywood matrix	Face	Core	Back
Type 1	Woven	Woven	Woven
Type 2	Woven	Unwoven	Woven
Type 3	Unwoven	Woven	Unwoven

Thickness Swelling

The specimens sized of 50 mm × 50 mm were cut according to Malaysia Standard (MS) 1787 Part A (2005a). They were ballasted and submerged in distilled water for different periods of 24, 48, 72 and 96 hours. The thickness swelling was measured as the following formulae:

Thickness swelling (%): $((T_2 – T_1)/T_1) \times 100$

Where;

T1 = initial thickness before soaking

T2 = final thickness after soaking

Static Bending

The specimens sized of 250 mm × 50 mm were cut according to MS 1787 Part B (2005b) and were tested using Instron Universal Testing Machine, at the speed rate of 4 mm/minute.

Results and Discussion

Thickness Swelling

As shown in Table 3, the thickness swelling was significantly different by a plywood matrix; but not for split width and a combination of matrix layer and split width. In plywood matrix, the thickness swelling was significantly different for all submerged period, except for 72 hours. As shown in Table 4, the averages thickness swelling were increased with increasing submerge period with regardless of plywood matrix and split width, ranging from 1.03% to 2.17% (Type 1), 1.14% to 2.38% (Type 2) and 1.35% to 2.79% (Type 3).

As shown in Figure 2; Type 1 (1.03%) plywood had a significantly lowest thickness swelling after 24 hours; followed by Types 2 (1.14%) and 3 (1.35%). A same trend was obtained after 48 hour, the Type 1 (1.66%) plywood had a significantly lower thickness swelling than those of Types 2 (1.74%) and 3 (2.15%). The averages thickness swelling was not significantly different for any plywood matrix; ranging from 2.09 % to 2.26 % after 72 hour. The Type 1 (2.17%) plywood had a significantly lowest thickness followed by types 2 (2.38%) and 3 (2.79%) after 96 hours.

Regardless of split width as shown in Figure 3, they

were ranged from 1.12% to 1.21% after 24 hours, from 1.84% to 1.87% after 72 hours and from 2.35% to 2.50% after 96 hours. Overall, the thickness swelling for all submerge period (except for 72 hours) was lowest in Type 1 plywood using 20 mm split width (Table 4).

TABLE 3. SUMMARIES OF THE ANALYSIS OF VARIANCES ON THE EFFECTS OF PLYWOOD MATRIX AND SPLIT WIDTH ON THE THICKNESS SWELLING.

Source	Time (hour)	DF	F	Significant
Plywood matrix (A)	24	2	3.30	0.06*
	48	2	3.26	0.06*
	72	2	2.61	0.10^{NS}
	96	2	3.45	0.05*
Split Width (B)	24	2	3.34	0.72^{NS}
	48	2	0.01	0.99^{NS}
	72	2	0.43	0.66^{NS}
	96	2	0.25	0.78^{NS}
(A)*(B)	24	4	0.66	0.63^{NS}
	48	4	0.58	0.68^{NS}
	72	4	0.98	0.45^{NS}
	96	4	0.31	0.85^{NS}

DF- degree of freedom, F – distribution, Sig – significance, Ns – is not significant, * is significant at 0.1.

TABLE 4. THE OVERALL AVERAGE OF THICKNESS SWELLING

Plywood matrix	Split width	24	48	72	96
Type 1	15	0.98(0.11)	1.59(0.58)	1.86(0.43)	2.14(0.55)
	20	0.93(0.19)	1.56(0.40)	1.92(0.44)	2.09(0.42)
	25	1.20(0.31)	1.84(0.28)	2.38(0.07)	2.28(0.40)
	Average	1.03(0.22)	1.66(0.40)	2.05(0.40)	2.17(0.41)
Type 2	15	1.03(0.20)	1.61(0.31)	1.83(0.34)	2.10(0.44)
	20	1.23(0.06)	1.83(0.14)	2.29(0.16)	2.54(0.37)
	25	1.17(0.30)	1.78(0.20)	2.07(0.23)	2.49(0.48)
	Average	1.14(0.31)	1.74(0.22)	2.06(0.30)	2.38(0.43)
Type 3	15	1.35(0.51)	2.31(0.90)	2.57(0.90)	2.81(0.83)
	20	1.44(0.23)	2.22(0.16)	2.52(0.22)	2.87(0.15)
	25	1.27(0.24)	1.93(0.44)	2.32(0.56)	2.69(0.64)
	Average	1.35(0.31)	2.15(0.53)	2.47(0.55)	2.79(0.53)

The paranthesis is standard deviation.

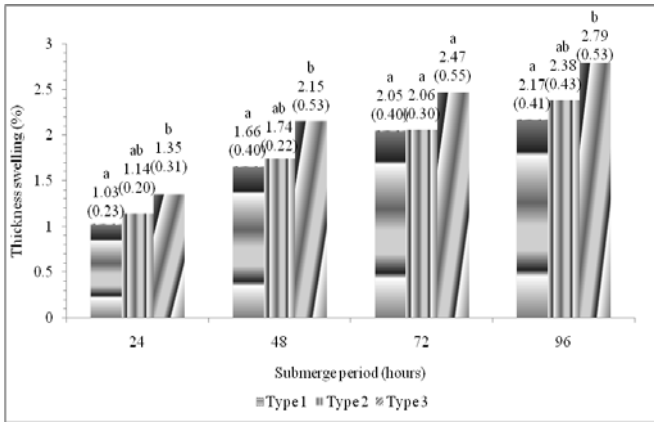

Means followed by the same letter(s) in the same column are not significantly different at the 0.05 probability level according to Waller-Duncan test.

FIGURE 2. THE THICKNESS SWELLING FROM DIFFERENT TYPE OF PLYWOOD MATRIX.

For comparison, the thickness swelling of oil palm plywood (7.7 mm thick) made with phenol formaldehyde after 24 hours'submergence was 10.59% (Hasmawi et al., 2014). The oil palm plywood pre-treated with LMWPF and pressed into 10 mm thick had the lowest thickness swelling of 4.76% after 24 hours' submergence period (Hoong et al., 2012).

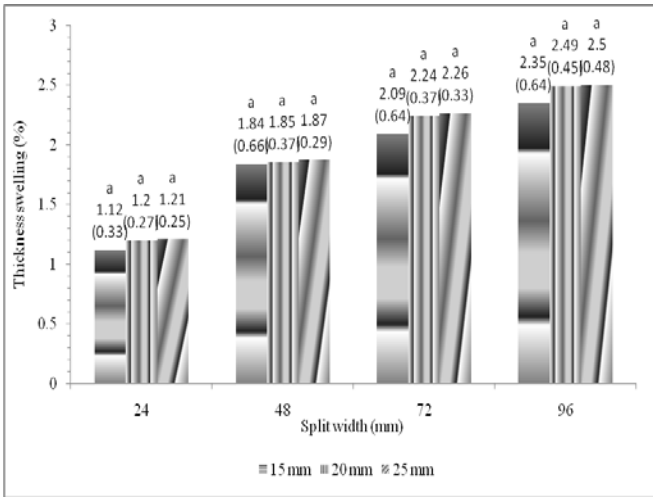

Means followed by the same letter(s) in the same column are not significantly different at the 0.05 probability level according to Waller-Duncan test.

FIGURE 3. THE THICKNESS SWELLING FROM DIFFERENT SPLIT WIDTH.

Static Bending Properties

The static bending, both MoR or MoE were significantly different by plywood matrix, but not for split width and a combination of plywood matrix and split width (Table 5). As shown in Figures 4 and 6; Type 3 plywood had a significantly highest MoR (79.88 Mpa) and MoE (7875.0 MPa) compared to other plywood matrix. The averages MoR and MoE of Type 1 plywood (33.88 MPa and 2979.4 MPa) were not significantly different with Type 2 plywood (33.24 MPa and 3136.5 MPa) respectively. The averages of MoR and MoE were also not significantly different with split width, ranging from 49.03 MPa to 51.19 MPa and from 4235.2 to 5190.0 MPa (Figures 5 and 7). Overall, the highest MoR (84.77 MPa) and MoE (8337.4 Mpa) was obtained in Type 3 plywood using 25 mm split width (Table 6). The averages of MoR and MoE obtained in this study were higher than 13 mm thick of LMWPF treated oil palm plywood (66.6 MPa and 7325 Mpa) as reported by Loh *et al.* (2010). The MoR and MoE of LMWPF pre-treated oil palm plywood (10 mm thick) pressed at 20 bar for the first 5 minute followed by 50 bar for the next 9 minute were 53.4 MPa and 5813 MPa respectively (Hong et al. 2012).

TABLE 5. SUMMARIES OF THE ANALYSIS OF VARIANCES ON THE EFFECTS OF PLYWOOD MATRIX AND SPLIT WIDTH ON THE STATIC BENDING

Source	Static bending	DF	F	Significant
Plywood matrix (A)	Modulus of rupture	2	80.7	0.00*
	Modulus of elasticity	2	55.8	0.00*
Split Width (B)	Modulus of rupture	2	2.5	0.12^{NS}
	Modulus of elasticity	2	0.4	0.69^{NS}
(A)*(B)	Modulus of rupture	4	2.1	0.13^{NS}
	Modulus of elasticity	4	1.4	0.26^{NS}

DF- degree of freedom, F – distribution, Sig – significance, Ns – is not significant, * is significant at 0.05

TABLE 6. THE OVERALL AVERAGES OF THICKNESS SWELLING

Plywood matrix	Split width	MoR	MoE
Type 1	15	33.92 (1.23)	2692.3 (480.2)
	20	39.06 (8.24)	3861.4 (928.4)
	25	28.67 (3.17)	2384.6 (466.3)
	Average	33.88 (6.33)	2979.4 (884.8)
Type 2	15	41.06 (1.75)	3726.1 (120.3)
	20	31.76 (12.76)	3699.7 (831.1)
	25	26.89 (4.53)	1983.7 (373.5)
	Average	33.24 (9.24)	3136.5 (979.2)
Type 3	15	72.11 (8.85)	7278.7 (2124.4)
	20	82.76 (25.87)	8008.8 (2477.8)
	25	84.77 (4.93)	8337.4 (3099.0)
	Average	79.88 (15.09)	7875.0 (2529.0)

The parenthesis is standard deviation.

Conclusions

The plywood matrix influenced the physical and static bending properties of woven oil palm plywood. The combination of three layers of woven oil palm plywood (Type 1) gave the lowest thickness swelling regardless of submerging period. In contrast, the arangement of woven veneer as core layer combined with unwoven face and back layers (Type 3) gave the highest static bending properties.

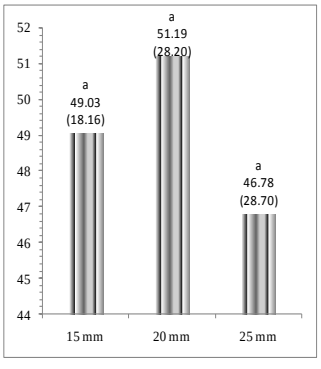

FIG 4. THE MOR FROM DIFFERENT TYPE OF PLYWOOD MATRIX

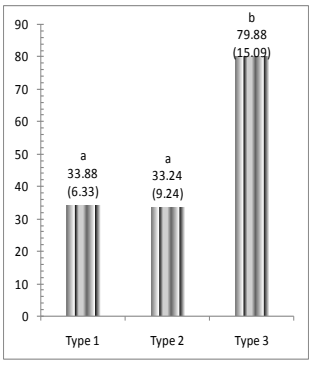

FIG 5. THE MOR FROM DIFFERENT SPLIT WIDTH.

Means followed by the same letter(s) in the same column are not significantly different at the 0.05 probability level according to Waller-Duncan test

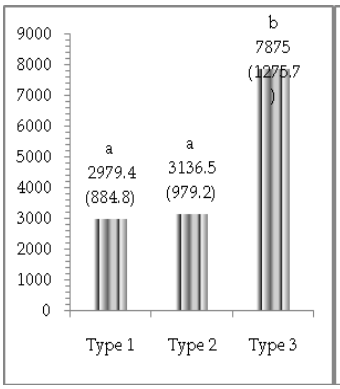

FIG 6. THE MOE FROM DIFFERENT TYPE OF PLYWOOD MATRIX

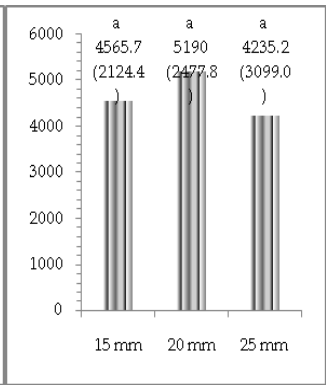

FIG 7. THE MOE FROM DIFFERENT SPLIT WIDTH.

Means followed by the same letter(s) in the same column are not significantly different at the 0.05 probability level according to Waller-Duncan test

REFERENCES

Abdul Khalil H. P. Shawkataly, Bhat IrshadulHaq,Sartika Mohamad Yusof. "Degradation, mechano-physical, and morphological properties of empty fruit bunch reinforced polyester composites." Journal of Bioresource (2010): 5(4): 2278-2296.

Abdul Khalil H. P. Shawkataly, Nurul Fazita Mohammad Rawi,Bhat Aamir Hussain, Mohammad Jawaid, and Nik Fuad Nik Abllah. "Development and material properties of new hybrid plywood from oil palm biomass." Journal of materials and Design (2010): 31(1):417-424.doi:10.1016/j.matdes.2009.05.040.

Anis Mokhtar, Kamarudin Hassan, Astimar Abdul Aziz, and MohdBasri Wahid. "Plywood from oil palm trunks." Journal of Oil Palm Research (2011): 23, 1159-1165.

Che Ku Abdullah, Mohammad Jawaid, Abdul Khalil H. P. Shawkataly, Zaidon Ashaari, and Anne Hadiyane. "Oil palm trunk polymer composites, morphology/water absorption and thickness swelling behaviour." Journal of Bioresource (2012): 7(3): 2948-2959.

Hasmawi Khalid, Zakiah Ahmad, Paridah Md. Tahir, and JamaludinKasim. "Effect of veneer treatment with phenol formaldehyde on dimensional stability and mechanical properties of oil palm stem (OPS) plywood." IACSIT International Journal of Engineering and Technology (2014): 6 (1): 76-80. doi:10.7763/IJET. 2014.V6.669

Maya Jacob, Sabu Thomas, and Konnanilkunnathal Thomas Varughese. "Mechanical properties of sisal/oil palm

hybrid fiber reinforced natural rubber composites." Journal of Composites Science and Technology (2004): 64: 955-965. doi:10.1016/S0266-3538(03)00261-6.

Mohamad Husin,Anis Mokhtar, and Wan Hasamudin Wan Hassan. "Energizing the wood-based industry in Malaysia. In: Proceedings of the 6th national seminar on the utilization of oil palm tree." Malaysia: Oil Palm Tree Utilization Committee (OPTUC) (2005): p. 6–13.

Mohd Shukri Mat Rasat, Razak Wahab, Othman Sulaiman, Janshah Moktar, Aminuddin Mohamed, Tamer A. Tabet, and Izyan Khalid. "Properties of composite boards from oil palm frond agricultural waste." Journal of Bioresource (2011): 6(4): 4389-4403.

Mohd Shukri Mat Rasat, Razak Wahab, Zulhisyam Abdul Kari, Ag Ahmad MohdYunus, Janshah Moktar, and Sitti Fatimah Mhd. Ramle. "Strength properties of bio-composite lumbers from lignocelluloses of oil palm fronds agricultural residue." International Journal on Advance Science, Engineering and Information Technology (2013): 3(3): 9-19.

MS 1787. 2005a. Wood based panel: Determination of thickness swelling after immersion in water (Part 6). Standard Industrial Research Institution of Malaysia.

MS 1787. 2005b. Wood based panel: Determination of modulus elasticity in bending and of bending strength (Part 10). Standard Industrial Research Institution of Malaysia.

Rokiah Hashim, Siti Norbain Sarmin, Othman Sulaiman, and LiliHanum Md. Yusof. "Effects of cold setting adhesives on properties of laminated veneer lumber from oil palm trunks in comparison with rubberwood." Eur. J. Wood Prod. (2011):69: 53-61.doi:10.1007/s00107-009-0405-2.

Rokiah Hashim, Wan Noor Aidawati Wan Nadhari, Othman Sulaiman, Salim Hiziroglu, Masatoshi Sato, Fumio Kawamura, Tay Guang Seng, Tomoko Sugimoto, and Ryohei Tanaka. "Evaluations of some properties of exterior particleboard made from oil palm biomass." Journal of Composite Materials (2010): 45: 1659-1665. doi:10.1177/0021998310385028.

Yeoh Beng Hoong, Yueh Feng Loh, Nor Hafiza Abd. Wahab, Paridah Md. Tahir, and Harun Jalaluddin. "Development of a new pilot scale production of high grade oil palm plywood: effect of pressing pressure." Journal of Materials and Design (2012): 36: 215 – 219. doi:10.1016/j. matdes.2011.10.004

Yueh Feng Loh, Paridah Md. Tahir, Yeoh Beng Hoong, Edi Suhaimi Bakar, Husain Hamdan, and AnisMokhtar. "Properties enhancement of oil palm plywood through veneer pretreatment with low molecular weight phenol formaldehyde resin." Journal of adhesion science and technology(2010): 2(8-10): 1729-1738. doi:10.1163/ 016942410X507795.